Single shot prediction of parametric partial differential equations

Khalid Rafiq¹

Department of Mechanical Engineering

University of Nevada, Reno

Reno, USA

krafiq@unr.edu

Wenjing Liao²

School of Mathematics

Georgia Institute of Technology

Atlanta, USA

wliao60@gatech.edu

Aditya G. Nair³

 $Department\ of\ Mechanical\ Engineering$

University of Nevada, Reno

Reno, USA

adityan@unr.edu

Abstract

We introduce Flexi-VAE, a data-driven framework for efficient single-shot forecasting of nonlinear parametric partial differential equations (PDEs), eliminating the need for iterative time-stepping while maintaining high accuracy and stability. Flexi-VAE incorporates a neural propagator that advances latent representations forward in time, aligning latent evolution with physical state reconstruction in a variational autoencoder setting. We evaluate two propagation strategies, the Direct Concatenation Propagator (DCP) and the Positional Encoding Propagator (PEP), and demonstrate, through representation-theoretic analysis, that DCP offers superior long-term generalization by fostering disentangled and physically meaningful latent spaces. Geometric diagnostics, including Jacobian spectral analysis, reveal that propagated latent states reside in regions of lower decoder sensitivity and more stable local geometry than those derived via direct encoding, enhancing robustness for long-horizon predictions. We validate Flexi-VAE on canonical PDE benchmarks, the 1D viscous Burgers' equation and the 2D advection-diffusion equation, achieving accurate forecasts across wide parametric ranges. The model delivers over $50 \times \text{CPU}$ and $90 \times \text{GPU}$ speedups compared to autoencoder-LSTM baselines for large temporal shifts. These results position Flexi-VAE as a scalable and interpretable surrogate modeling tool for accelerating high-fidelity simulations in computational fluid dynamics (CFD) and other parametric PDE-driven applications, with extensibility to higher-dimensional and more complex systems.

1 Introduction

Parametric partial differential equations (PDEs) are essential tools for modeling physical systems where spatio-temporal dynamics are influenced by parameters such as material properties, boundary

conditions, or flow characteristics. These equations are expressed as:

$$\frac{\partial \boldsymbol{u}}{\partial t} = f\left(\boldsymbol{x}, \boldsymbol{u}, \nabla_{\boldsymbol{x}} \boldsymbol{u}, \nabla_{\boldsymbol{x}}^2 \boldsymbol{u}, \dots; \boldsymbol{\zeta}\right),\tag{1}$$

where u represents the system state, f is the nonlinear evolution function that depends on the state and its higher-order spatial derivatives, and ζ denotes the shape, material or operational parameter(s) governing the dynamics of the system, such as the Reynolds number (Re) or flexural rigidity.

Traditional numerical solvers, including finite element (FEM) [73] and finite volume methods (FVM) [47], solve Eq. (1) by iteratively computing solutions for each parameter value ζ . However, these traditional approaches become computationally prohibitive when dealing with high-dimensional parameter spaces or simulations over long time horizons. The iterative nature of these solvers, coupled with the need to compute solutions at multiple time steps, amplifies computational costs due to truncation errors from discretization and round-off errors from numerical precision [56]. For parametric studies (e.g., varying Re), this often necessitates re-solving the PDE from scratch, limiting real-time applicability in control or optimization tasks.

To alleviate the computational burden of high-dimensional PDE simulations, model reduction techniques seek to approximate the full system dynamics in a lower-dimensional subspace. One such approach is Proper Orthogonal Decomposition (POD)[7, 26, 45, 61], which extracts spatial modes from simulation data, providing an optimal basis for capturing energetic flow structures. Similarly, Dynamic Mode Decomposition (DMD) and its extensions[57, 32, 64, 33] offer a data-driven alternative by identifying single-frequency spatio-temporal structures through a linear operator framework. While DMD excels at uncovering recurrent dynamical features, it often struggles with highly nonlinear dynamics and lacks generalizability to unseen parameter regimes.

Building on these modal decomposition techniques, projection-based reduced-order models (ROMs) approximate high-dimensional PDE dynamics in a low-dimensional subspace by projecting the governing equations onto a small set of dominant spatial modes. For example, applying Galerkin projection (GP)[55] to Proper Orthogonal Decomposition (POD) modes of the Navier–Stokes equations results in a reduced system of ordinary differential equations that approximates the full PDE dynamics. However, truncating to a limited number of dominant modes often leads to instabilities and inaccuracies in long-time horizon predictions, as the neglected modes—though energetically less significant—can still play a critical role in nonlinear energy transfer and system dynamics [2]. Kalman filter extensions[27, 68, 66, 13, 22] employ statistical estimation techniques to track system states but typically rely on assumptions of linearity or Gaussian noise.

Unsupervised machine-learning approaches based on autoencoders (AEs) [24] have recently emerged as powerful alternatives for nonlinear model reduction for developing efficient ROMs [5, 15, 43, 71, 19, 69]. By leveraging deep neural networks with nonlinear activation functions, AEs learn low-dimensional representations that capture complex dynamical behaviors beyond the reach of linear reduction techniques [5, 52, 48, 54]. An approximation and generalization analysis was provided in Liu et al. [37] for AE-based operator learning to demonstrate its sample efficiency when the input data lie on a low-dimensional manifold. Early studies by Milano and Koumoutsakos [46] demonstrated the efficacy of such networks on canonical fluid mechanics problems, including the Burgers equation and turbulent channel flow, while emphasizing conceptual similarities and differences between AEs and POD. Subsequent work has further exploited the high compression ratio and inherent nonlinearity of AEs, often combining them with sequential models such as long short-term memory (LSTM) [25] or reservoir computing [20] or the transformer [67] architectures to evolve latent states over time [50, 63, 44, 14, 62]. For instance, in Maulik et al. [44], the authors compared a POD-Galerkin ROM against an AE-LSTM approach for viscous Burgers equation and

the shallow water equation, highlighting not only the superior accuracy of the deep-learning-based method, but also the flexibility to incorporate PDE parameters as additional features in a parametric LSTM model. Despite these advances, most AE-based frameworks still separate latent encoding from temporal propagation and rely on iterative predictions for multi-step forecasts. This leaves open the question of how to perform single-shot forecasting directly in latent space, enabling more efficient and scalable predictions across a broader range of parametric settings.

Neural operator learning has introduced an alternative paradigm for data-driven PDE modeling by directly learning mappings between function spaces. Approaches such as Fourier Neural Operators (FNO) [36] and DeepONet [41] bypass traditional time-stepping by directly mapping input function spaces to output function spaces, allowing for global predictions across spatial and temporal domains. These models operate in high-dimensional state space without explicitly reducing dimensionality, making them computationally demanding for large-scale problems.

Generative models, particularly Variational Autoencoders (VAEs) [30] have been widely used for sequential modeling, with several extensions developed to capture temporal dynamics. The Kalman Variational Autoencoder (KVAE) [18] integrates Kalman filters with VAEs for efficient inference of linear latent dynamics. The Recurrent Variational Autoencoder (RVAE) [10] combines VAEs with recurrent neural networks (RNNs) to model temporal dependencies but relies on recursive forecasting, limiting its one-shot prediction capabilities. Disentangled Sequential Autoencoders (DSAE) [35] offer more structured representations by separating static and dynamic latent factors, improving the interpretability of time-series data. Beyond these models, VAEs have also been combined with physics-informed neural networks (PINNs) [53] to model stochastic differential equations [72], though such approaches require explicit knowledge of governing equations, making them less suitable for systems with unknown dynamics. Importantly, VAEs offer two significant advantages: the ability to incorporate inductive biases from physical knowledge and a simple latent space structure that facilitates evaluation of these biases for interpretability [17].

When data or machine learning tasks exhibit low-dimensional geometric structures, it has been demonstrated that deep learning can adapt to the low-dimensional geometric structures even when these structures are unknown [9, 49, 59, 37]. When data lie on a low-dimensional manifold, the approximation error of neural networks scales in a power law of the network size where the power depends on the intrinsic dimension of the manifold [8]. When a finite number of samples are used to learn these regular functions, the generalization error scales in a power law of the sample size where the power depends on the intrinsic dimension of the manifold [9, 49]. When AEs are applied for data on a low-dimensional manifold, the reconstruction error is guaranteed if the network architecture is properly chosen [38]. These works demonstrate that deep learning approaches are capable of leveraging model efficiency and sample efficiency in machine learning tasks.

Our work builds upon recent advances in constraining latent dynamics of PDE-governed systems using geometric and physics-based priors. For example, Lopez et al. [39, 40] developed manifold-constrained VAEs that encode nonlinear PDE dynamics into geometrically structured latent spaces, while Glyn-Davies et al. [21] integrated data assimilation with physics-informed latent dynamics, enabling joint inference of system states and parameters. These approaches are effective in regularizing latent trajectories and embedding observational data into physically meaningful representations. However, they primarily focus on modeling dynamics within a fixed parameter regime and rely on recurrent temporal inference, which limits scalability and generalization across varying physical conditions.

To overcome these limitations, we introduce a parametric neural latent propagator that eliminates recurrent updates by directly predicting the system's future evolution over multiple time steps in a single evaluation, starting from a single high-dimensional input state. This single-shot forecasting approach significantly enhances computational efficiency by avoiding sequential rollouts,

while maintaining accuracy over long horizons and enabling generalization across unseen parameter regimes.

To enable this, we develop a flexible variational autoencoder framework—Flexi-VAE—that integrates a propagator network to advance latent representations through time, incorporating the parameters of the PDE to align with the system's physical evolution. We investigate two distinct propagation strategies for modeling latent dynamics: a direct concatenation approach, referred to as the Direct Concatenation Propagator (DCP), and a high-dimensional embedding method using positional encodings, termed the Positional Encoding Propagator (PEP). These designs are evaluated with respect to their ability to model parametric latent evolution in a single shot.

Our comparative analysis highlights the trade-offs between data efficiency, generalization capability, model complexity, and physical interpretability within the latent forecasting framework. We validate our approach on two benchmark PDE systems: the nonlinear one-dimensional Burgers equation and the two-dimensional advection-diffusion equation, demonstrating accurate and stable long-term forecasts across a wide range of parametric conditions. The methodology is presented in §2.1 followed by results and analysis in §3, and concluding discussions are offered in §4.

To facilitate broader use and reproducibility, we provide access to our implementation on **GitHub**¹ and host an interactive demo on **Hugging Face Spaces**².

2 Flexi-VAE from a Geometric Perspective

2.1 Methodology

The goal is of this paper is to forecast the solution $u(x, t+\tau, \zeta)$ given the current solution $u(x, t, \zeta)$ of the parametric PDE in Eq. (1):

$$u(x,t,\zeta) \Longrightarrow u(x,t+\tau,\zeta)$$

Here $\boldsymbol{x} \in \mathbb{R}^n$ represents the spatial grid for the sampling of the PDE solution, t denotes the current time, τ denotes a prescribed predictive time horizon and $\boldsymbol{\zeta}$ includes parametric inputs such as initial or boundary conditions or other non-dimensional quantities. Suppose the training dataset is constructed from K distinct parameter configurations $\{\boldsymbol{\zeta}_k\}_{k=1}^K$. For each configuration $\boldsymbol{\zeta}_k$, we collect J distinct initial conditions $\{t_{kj}\}_{j=1}^J$, and for each initial time t_{kj} , we consider I different predictive horizons $\{\tau_{kji}\}_{i=1}^I$. This results in a set of solution snapshots of the form $\{\boldsymbol{u}(\boldsymbol{x},t_{kj},\boldsymbol{\zeta}_k), \ \boldsymbol{u}(\boldsymbol{x},t_{kj}+\tau_{kji},\boldsymbol{\zeta}_k)\}$ for $i=1,\ldots,I$ and $j=1,\ldots,J$. We denote the full training dataset as:

$$\mathcal{D} := \{ (\boldsymbol{u}(\boldsymbol{x}, t_{kj}, \boldsymbol{\zeta}_k), \ \boldsymbol{u}(\boldsymbol{x}, t_{kj} + \tau_{kji}, \boldsymbol{\zeta}_k)) : i = 1, \dots, I; \ j = 1, \dots, J \}_{k=1}^K.$$

Forecasting the solution in the high-dimensional space typically requires explicit knowledge of the governing physics or the training of a large-scale neural network with a large amount of data [28, 63, 44, 14]. In many science and engineering applications, the solutions of parametric PDEs often reside on or near low-dimensional geometric structures embedded in high-dimensional ambient spaces [11]. These structures arise due to underlying physical constraints and the parametric dependence of the PDE. As a result, despite the apparent complexity and high dimensionality of the solution space, the essential variation can often be captured by a relatively small number of degrees of freedom. This phenomenon motivates us to build data-driven approaches to exploit the intrinsic low-dimensionality to achieve efficient prediction of the PDE solutions across a wide range of parameter values.

 $^{^{1} \}mathtt{https://github.com/Khalid-Rafiq-01/Flexi-VAE}$

²https://huggingface.co/spaces/krafiq/Flexi-VAE

In this paper, we employ a variational autoencoder (VAE) [30] to encode high-dimensional solutions of partial differential equations (PDEs), denoted as $\boldsymbol{u}(\boldsymbol{x},t,\boldsymbol{\zeta}) \in \mathbb{R}^n$, into a low-dimensional probabilistic latent space $\tilde{\boldsymbol{z}}(t,\boldsymbol{\zeta}) \in \mathbb{R}^m$, where m is the latent dimension and $\tilde{\cdot}$ denotes an approximated numerical representation. Instead of predicting the solution $\boldsymbol{u}(\boldsymbol{x},t+\tau,\boldsymbol{\zeta}) \in \mathbb{R}^n$ in the high-dimensional ambient space, we make a prediction in the latent space, and then decode to the ambient space.

The VAE comprises an encoder \mathcal{E}_{θ_e} and a symmetric decoder \mathcal{D}_{θ_d} , which together define a probabilistic model. The encoder maps the input field to a posterior distribution $p_{\theta_e}(\boldsymbol{z}|\boldsymbol{u})$ from which latent variables $\tilde{\boldsymbol{z}}$ are sampled. Sampling is performed using the reparameterization trick, enabling end-to-end gradient-based optimization. The decoder \mathcal{D}_{θ_d} reconstructs the solution $\tilde{\boldsymbol{u}}(\boldsymbol{x},t,\boldsymbol{\zeta})$ from these latent samples. In our implementation, both the encoder and decoder utilize convolutional layers and group normalization, which enhance representation quality and training stability.

A standard Gaussian prior $p_{\theta}(z)$ is imposed on the latent space, and the discrepancy between the posterior and prior is penalized using the Kullback–Leibler (KL) divergence:

$$D_{\mathrm{KL}}\left(p_{\theta_e}(\boldsymbol{z}|\boldsymbol{u}),\ p_{\theta}(\boldsymbol{z})\right).$$

in addition to a reconstruction loss that minimizes the error between \boldsymbol{u} and $\tilde{\boldsymbol{u}}$.

To model temporal evolution or parametric dependencies, we incorporate a single-shot forecasted solution $\hat{\boldsymbol{u}}(\boldsymbol{x},t+\tau,\boldsymbol{\zeta})$ (where $\hat{\cdot}$ denotes forecasted approximate numerical representation) that advances the solution forward in time by a prescribed horizon τ . Unlike sequential autoregressive models that propagate the state step-by-step, our approach performs forecasting in a single evaluation, reducing both computational cost and error accumulation across time steps.

The total loss function used for training incorporates three components: a reconstruction loss to ensure fidelity in encoding-decoding, a KL divergence regularization term to enforce structured latent representations, and a propagated reconstruction loss to promote temporal or parametric consistency in the prediction. The loss is defined as

$$\mathcal{L}(\mathcal{D}) = \underbrace{\frac{1}{KJ} \sum_{k=1}^{K} \sum_{j=1}^{J} \|\mathbf{u}(\mathbf{x}, t_{kj}, \boldsymbol{\zeta}_{k}) - \mathcal{D}_{\theta_{d}} \circ \mathcal{E}_{\theta_{e}} (\mathbf{u}(\mathbf{x}, t_{kj}, \boldsymbol{\zeta}_{k}))\|^{2} - \beta \underbrace{\mathcal{D}_{KL}(p_{\theta_{e}}(\mathbf{z}|\mathbf{u}), p_{\theta}(\mathbf{z}))}_{KL \text{ Divergence Regularization}}$$

$$+ \eta \underbrace{\frac{1}{KJI} \sum_{k=1}^{K} \sum_{j=1}^{J} \sum_{i=1}^{I} \|\mathbf{u}(\mathbf{x}, t_{kj} + \tau_{kji}, \boldsymbol{\zeta}_{k}) - \hat{\mathbf{u}}(\mathbf{x}, t_{kj} + \tau_{kji}, \boldsymbol{\zeta}_{k})\|^{2}}_{Propogator Loss}.$$
(2)

where β is a regularization parameter that controls the trade-off between reconstruction accuracy and the latent space disentanglement in the β -VAE formulation [23], while η weighs the relative importance of the forecasted reconstruction term. Increasing β promotes more structured latent representations at the cost of reconstruction accuracy [60]. Setting $\eta > 1$ emphasizes accurate forecasting, which is especially useful when downstream tasks involve long-horizon predictions or parametric generalization. For notational simplicity, we drop the detailed subscripts used in the loss function (e.g., t_{kj} , τ_{kji} , ζ_k) and refer generically to tuples as $(\boldsymbol{u}(\boldsymbol{x},t), \boldsymbol{u}(\boldsymbol{x},t+\tau), \tau, \zeta)$ throughout the remainder of this section.

Instead of predicting the PDE solution at time $t + \tau$ from time t in the ambient space, we propagate the latent embedding $\tilde{\boldsymbol{z}}(t,\boldsymbol{\zeta}) = \mathcal{E}_{\theta_e}(\boldsymbol{u}(\boldsymbol{x},t,\boldsymbol{\zeta}))$ using a feed-forward parametric neural propagator with learnable parameters θ_p , resulting in a discrete-time system:

$$\hat{\mathbf{z}}(t+\tau,\boldsymbol{\zeta}) = \mathcal{P}_{\theta_n}(\tilde{\mathbf{z}}(t,\boldsymbol{\zeta});\tau,\boldsymbol{\zeta}),\tag{3}$$

where the propagator \mathcal{P}_{θ_p} serves as a integrator of the low-dimensional latent dynamics over a time horizon of τ . In Eq. (3), $\tilde{\boldsymbol{z}}(t,\boldsymbol{\zeta}) = \mathcal{E}_{\theta_e}(\boldsymbol{u}(\boldsymbol{x},t,\boldsymbol{\zeta}))$ is the latent embedding of the PDE solution parametrized by $\boldsymbol{\zeta}$ at time t, and $\hat{\boldsymbol{z}}(t+\tau,\boldsymbol{\zeta})$ is the predicted latent embedding at time $t+\tau$. Our framework learns the propagated dynamics over multiple time horizons in a single shot.

The propagated latent variable \hat{z} is then decoded via \mathcal{D}_{θ_d} to reconstruct the high-dimensional forecast:

$$\hat{\boldsymbol{u}}(\boldsymbol{x}, t + \tau, \boldsymbol{\zeta}) = \mathcal{D}_{\theta_d}(\hat{\boldsymbol{z}}(t + \tau, \boldsymbol{\zeta})). \tag{4}$$

The overall idea of our single-shot prediction is shown in Fig. 1.

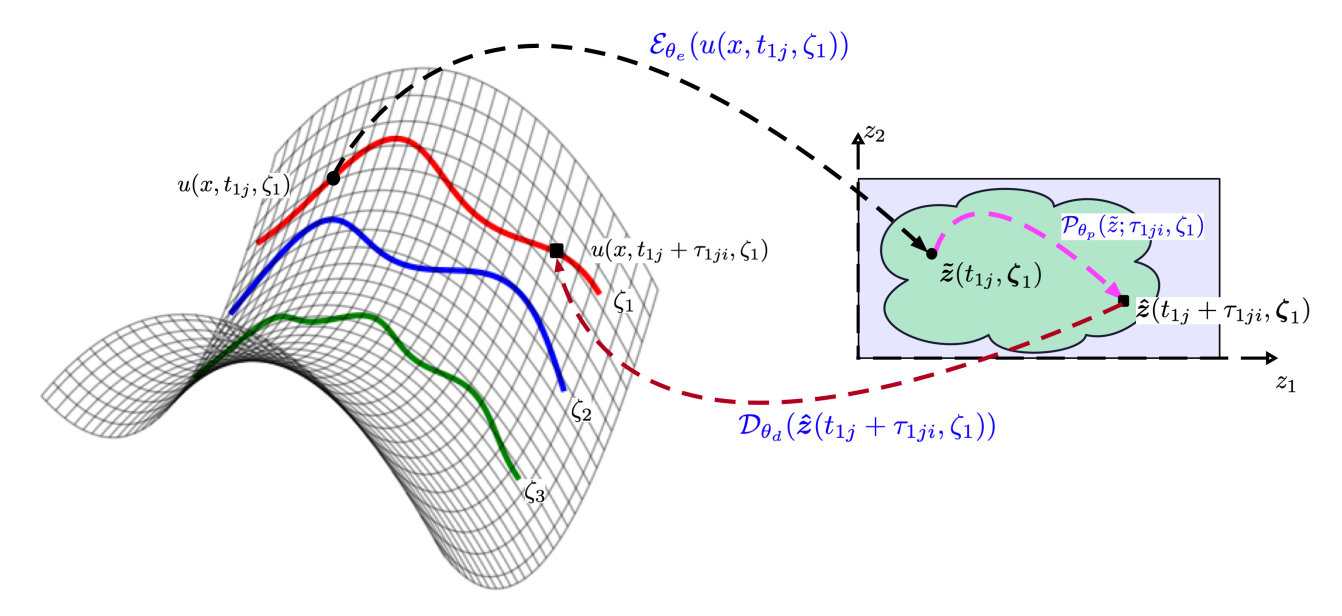


Figure 1: Conceptual overview of the Flexi-VAE framework for single-shot prediction. The highdimensional solution manifold $\mathcal{M} \subseteq \mathbb{R}^n$ is shown on the left, while the corresponding latent space $\mathbf{z} \subseteq \mathbb{R}^m$ is depicted on the right (illustrated here as a 2D manifold). Given an initial highdimensional state $\mathbf{u}(\mathbf{x}, t_{kj}, \boldsymbol{\zeta_k})$, the encoder \mathcal{E}_{θ_e} maps it to a low-dimensional latent representation $\tilde{\mathbf{z}}(t_{kj}, \boldsymbol{\zeta_k})$. Here, k refers to the parameter configuration and j refers to the initial condition. The latent state is then evolved forward in time by the propagator \mathcal{P}_{θ_p} (magenta arrow), conditioned on the forecasting horizon τ_{kji} and system parameters ζ_k , producing the propagated latent vector $\hat{\mathbf{z}}(t_{kj} + \tau_{kji}, \boldsymbol{\zeta_k})$. Here, i refers to the predictive time horizon. Finally, the shared decoder \mathcal{D}_{θ_d} forecasts the high-dimensional prediction $\hat{u}(\mathbf{x}, t_{kj} + \tau_{kji}, \boldsymbol{\zeta_k})$ from the propagated latent.

Notice that the propagated latent vectors are decoded using the same decoder employed for reconstructing the solution at the current time step. This architectural choice promotes parameter efficiency and enables robust long-horizon forecasting without increasing the model complexity. The overall architecture of our model, Flexi-VAE (Flexible Variational Autoencoder), is illustrated in Fig. 2.

To ensure that the propagator \mathcal{P}_{θ_p} effectively integrates both temporal evolution and parametric dependencies, we explore two distinct parameter-informed strategies. The first, the positional encoding propagator (PEP), encodes system parameters and temporal offsets into a structured high-dimensional embedding inspired by transformer architecture[67]. This is achieved by mapping parameters ζ and τ into an embedding space, where they interact nonlinearly with the latent representation. The enriched latent state is then projected back to the original dimension using a learnable transformation, preserving structured parameter interactions. In contrast, the direct concatenation propagator (DCP) offers a more explicit mechanism by appending system parameters directly to the latent vector. This approach leverages the assumption that the VAE's latent space already encodes meaningful representations of the system's dynamics, allowing direct parameter concatenation to guide the latent state evolution. Both the propagators, PEP and DCP are shown in Fig. 3.

In PEP, the system parameters ζ and temporal offsets τ are mapped to high-dimensional embeddings using sinusoidal functions, where frequencies $\omega_f = 1/10000^{2f/d}$ ensure smooth parameter

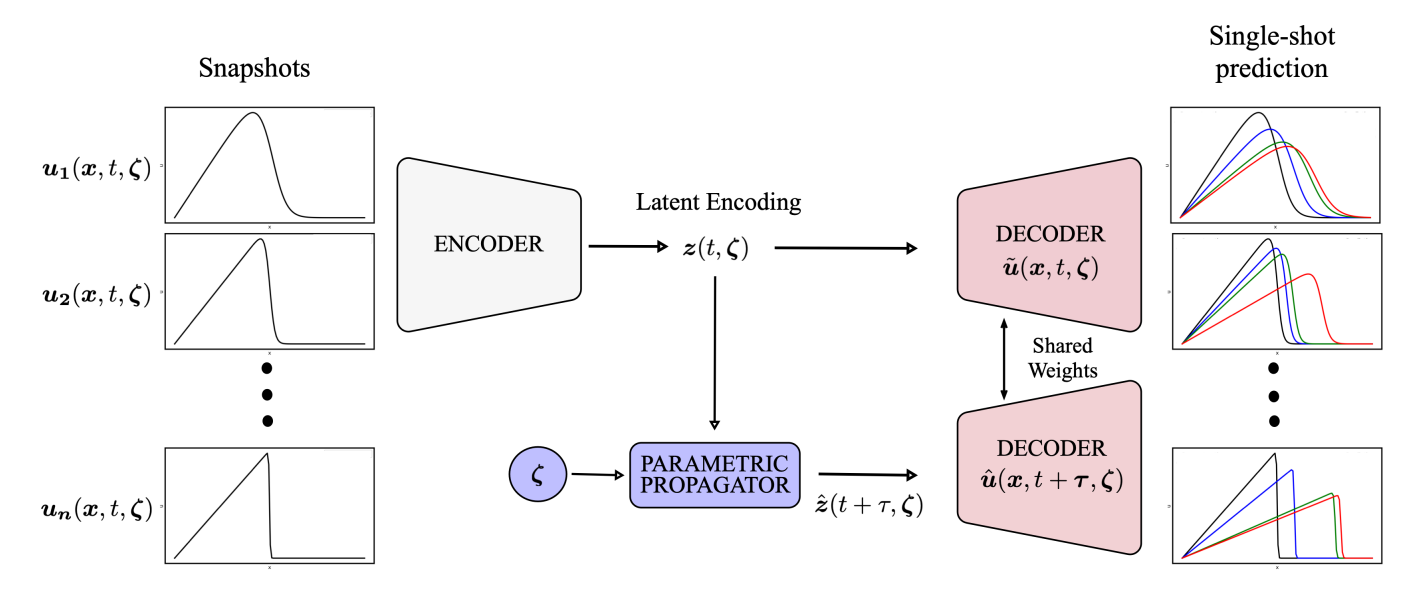


Figure 2: Schematic representation of the Flexi-VAE architecture. The encoder compresses the high-dimensional input into a low-dimensional latent space. The parametric neural propagator advances the latent state across multiple time steps, incorporating both temporal and parametric information. Finally, the shared decoder is used both to reconstruct the high-dimensional state from the latent vector at the current time step and to forecast the future high-dimensional state from the propagated latent representation.

encoding. The embedding dimension d is chosen such that d > m, providing sufficient capacity to represent variations of parameters in the latent space. Next, the latent vector $\tilde{\boldsymbol{z}}(t,\boldsymbol{\zeta}) \in \mathbb{R}^m$ is projected into \mathbb{R}^d using an up-projection function \mathcal{F}_{up} . The encoded parameter embeddings $PE(\boldsymbol{\zeta})$ and $PE(\tau)$ are incorporated via element-wise addition, yielding an enriched latent representation $\mathcal{F}_{up}(\tilde{\boldsymbol{z}}(t,\boldsymbol{\zeta})) + PE(\boldsymbol{\zeta}) + PE(\tau)$. The enriched latent is projected back to the original dimension using a down-projection function $\mathcal{F}_{down}: \mathbb{R}^d \to \mathbb{R}^m$, producing the propagated latent state $\hat{\boldsymbol{z}}(t+\tau,\boldsymbol{\zeta})$, which is then decoded to reconstruct the future state $\hat{\boldsymbol{u}}(\boldsymbol{x},t+\tau,\boldsymbol{\zeta})$. This approach allows PEP to efficiently integrate parametric variations while maintaining structured latent evolution.

DCP adopts a hypothesis-driven design by directly appending system parameters to the latent representation. The augmented latent vector is constructed as $[\tilde{z}(t,\zeta)||\zeta||\tau]$ and passed through a fully connected neural network $\mathcal{F}_{\text{concat}}$ to produce the propagated latent state $\hat{z}(t+\tau,\zeta)$. Since τ governs temporal progression and ζ influences physical characteristics of the system, DCP offers an interpretable and computationally efficient means of incorporating parametric dependencies. By reducing the complexity of parameter embedding, this approach alleviates the learning burden on $\mathcal{F}_{\text{concat}}$ and improves data efficiency. Both propagators facilitate one-shot multi-step forecasting while embedding parametric dependencies into the latent space. While PEP provides greater flexibility for modeling complex parameter interactions, DCP offers a more interpretable and computationally efficient alternative.

The effectiveness of our approach relies on learning optimal parameters for the encoder, decoder, and propagator networks, denoted as θ_e , θ_d , and θ_p , respectively. These parameters are optimized jointly using Adam [29] to minimize the total loss function in Eq. (2), which consists of reconstruction loss, KL divergence regularization, and propagated reconstruction loss. For PEP, θ_p include network weights of both the up-projection \mathcal{F}_{up} and down-projection \mathcal{F}_{down} functions. The weight η in Eq. (2) is tuned to prioritize either immediate reconstruction accuracy or long-horizon forecasting performance.

Fig. 4 summarizes the algorithm's core workflow, emphasizing the data transformation stages and shared components.

The overall algorithm is shown in Algorithm 1.

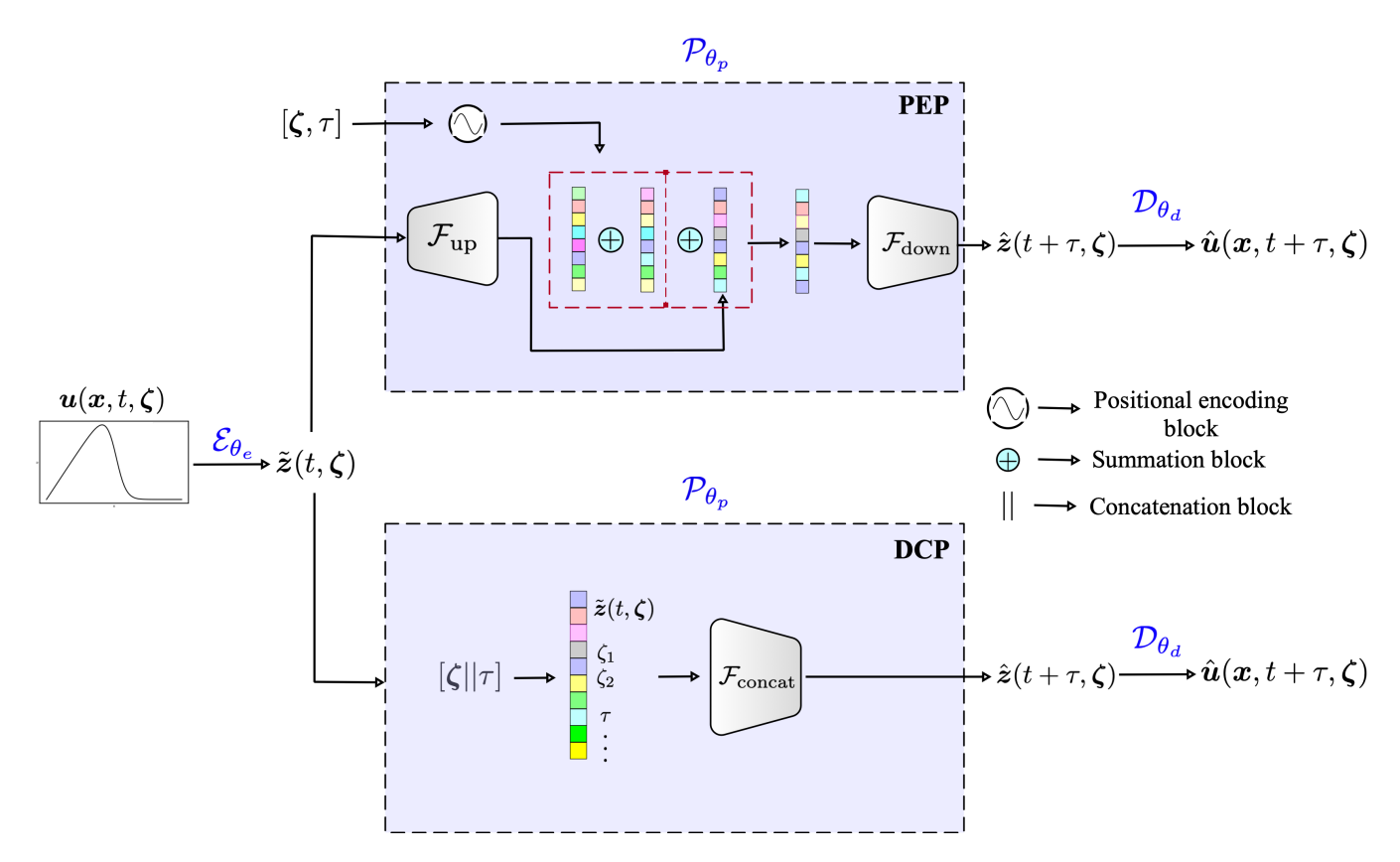


Figure 3: Comparison of two parameter-informed latent propagation strategies in the Flexi-VAE framework. Top: The Positional Encoding Propagator (PEP) maps the latent state $\tilde{z}(t,\zeta)$ to a higher-dimensional space via \mathcal{F}_{up} , where it is enriched with sinusoidal embeddings of the parameters ζ and time offset τ , followed by summation and down-projection through \mathcal{F}_{down} to yield the propagated latent $\hat{z}(t+\tau,\zeta)$. Bottom: The Direct Concatenation Propagator (DCP) concatenates $\tilde{z}(t,\zeta)$ with ζ and τ , and passes the augmented vector through a fully connected network \mathcal{F}_{concat} . In both approaches, the propagated latent is decoded by the shared decoder \mathcal{D}_{θ_d} to produce the forecasted physical state $\hat{u}(x,t+\tau,\zeta)$.

2.2 Geometric Representation of Flexi-VAE

Our latent-space forecasting framework is based on the manifold hypothesis, which assumes that the set of PDE solutions $\{u(x,t,\zeta)\}\subset\mathbb{R}^n$ lies on a compact, m-dimensional Riemannian manifold isometrically embedded in \mathbb{R}^n . The reconstruction term in the loss function in Eq.(2) enables unsupervised learning of this manifold through a low-dimensional latent representation. Meanwhile, the propagator loss supports supervised learning of the system's temporal evolution within the latent space. In this section, we provide a neural network representation theory about the unsupervised learning of the manifold structure and the supervised learning of the latent propagator in Flexi-VAE.

We consider feedforward neural networks (FNNs) with a nonlinear activiation function σ . An FNN with L layers is defined as

$$f(\boldsymbol{u}) = W_L \cdot \sigma \left(W_{L-1} \cdots \sigma(W_1 \boldsymbol{u} + \boldsymbol{b}_1) + \cdots + \boldsymbol{b}_{L-1} \right) + \boldsymbol{b}_L, \tag{5}$$

where W_i and \boldsymbol{b}_i denote the weight matrices and bias vectors, respectively, and σ is applied elementwise. When $\sigma(x) = \max(x, 0)$, the FNN is referred to as a ReLU network.

We define a class of neural networks with inputs in \mathbb{R}^{d_1} and outputs in \mathbb{R}^{d_2} as

 $\mathcal{F}_{\mathrm{NN}}(d_1,d_2;L,p,K,\kappa,R) = \{f: \mathbb{R}^{d_1} \to \mathbb{R}^{d_2} \mid f \text{ has the form of (5) with } L \text{ layers and width bounded by } p, \\ \|f\|_{L^{\infty}} \leq R, \sum_{i=1}^{L} \|W_i\|_0 + \|\boldsymbol{b}_i\|_0 \leq K, \\ \|W_i\|_{\infty,\infty} \leq \kappa, \|\boldsymbol{b}_i\|_{\infty} \leq \kappa \text{ for } i=1,...,L\},$

where $||H||_{\infty,\infty} = \max_{i,j} |H_{ij}|$ for a matrix H, $||\cdot||_0$ denotes the number of non-zero elements of its

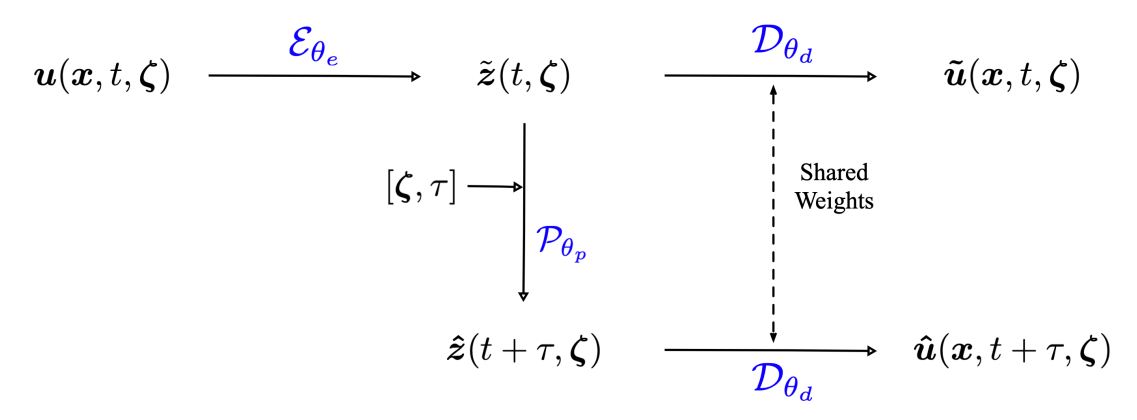


Figure 4: Overview of the Flexi-VAE architecture. The encoder \mathcal{E}_{θ_e} transforms the input state $\boldsymbol{u}(\boldsymbol{x},t,\boldsymbol{\zeta})$ into a latent representation $\tilde{\boldsymbol{z}}$. The propagator \mathcal{P}_{θ_p} evolves the latent state, conditioned on parameters $\boldsymbol{\zeta}$ and temporal offset τ . The decoder \mathcal{D}_{θ_d} reconstructs the instantaneous $\tilde{\boldsymbol{u}}(\boldsymbol{x},t,\boldsymbol{\zeta})$ and the propagated state $\hat{\boldsymbol{u}}(\boldsymbol{x},t+\tau,\boldsymbol{\zeta})$.

```
Algorithm 1: Training procedure for Flexi-VAE
      Input: Training dataset
                             \mathcal{D} := \{ (\boldsymbol{u}(\boldsymbol{x}, t_{kj}, \boldsymbol{\zeta}_k), \ \boldsymbol{u}(\boldsymbol{x}, t_{kj} + \tau_{kji}, \boldsymbol{\zeta}_k)) : i = 1, \dots, I; \ j = 1, \dots, J \}_{k=1}^K
                             Hyperparameters: \beta, \eta, learning rate \alpha, number of epochs E, batch size B
       Output: Trained parameters \theta_e, \theta_d, \theta_p
  1 Initialize network parameters: \theta_e, \theta_d, \theta_p
  2 for each epoch = 1 to E do
               for each mini-batch \mathcal{B} \subset \mathcal{D} of size B do
  3
                      Encoding:
  4
                       \boldsymbol{\mu}, \log \boldsymbol{\sigma}^2 \leftarrow \mathcal{E}_{\theta_e}(\boldsymbol{u}(\boldsymbol{x}, t, \boldsymbol{\zeta}))
  5
                      Sample: \tilde{z} \leftarrow \mu + \sigma \odot \epsilon, where \epsilon \sim \mathcal{N}(0, \mathbf{I})
  6
                       Reconstruction:
  7
                       \tilde{\boldsymbol{u}}(\boldsymbol{x},t,\boldsymbol{\zeta}) \leftarrow \mathcal{D}_{\theta_d}(\tilde{\boldsymbol{z}})
  8
                      Propagation:
  9
                      if using PEP then
10
                        \hat{z} \leftarrow \mathcal{F}_{\text{down}} \left( \mathcal{F}_{\text{up}}(\tilde{z}) + \text{PE}(\zeta) + \text{PE}(\tau) \right)
11
                      else if using DCP then
12
                        \hat{z} \leftarrow \mathcal{F}_{\text{concat}}\left(\left[\tilde{z}||\zeta||\tau\right]\right)
                      end
14
                      \hat{\boldsymbol{u}}(\boldsymbol{x},t+	au,\boldsymbol{\zeta}) \leftarrow \mathcal{D}_{\theta_d}(\hat{\boldsymbol{z}})
15
                      Loss computation:
16
                       L_{\mathrm{RE}} \leftarrow \|\boldsymbol{u}(\boldsymbol{x},t,\boldsymbol{\zeta}) - \tilde{\boldsymbol{u}}(\boldsymbol{x},t,\boldsymbol{\zeta})\|^2
17
                       L_{\text{PRE}} \leftarrow \|\boldsymbol{u}(\boldsymbol{x}, t + \tau, \boldsymbol{\zeta}) - \hat{\boldsymbol{u}}(\boldsymbol{x}, t + \tau, \boldsymbol{\zeta})\|^2
18
                      L_{\text{KL}} \leftarrow -\frac{1}{2} \sum_{j=1}^{m} \left(1 + \log \sigma_j^2 - \mu_j^2 - \sigma_j^2\right)  (Gaussian prior [31])
19
                       \mathcal{L} \leftarrow L_{\text{RE}} + \eta L_{\text{PRE}} + \beta L_{\text{KL}}
20
                       Gradient update:
21
                      \theta_e \leftarrow \theta_e - \alpha \nabla_{\theta_e} \mathcal{L} , \theta_d \leftarrow \theta_d - \alpha \nabla_{\theta_d} \mathcal{L}, \theta_p \leftarrow \theta_p - \alpha \nabla_{\theta_p} \mathcal{L}
22
               end
23
```

argument, and $||f||_{L^{\infty}}$ denotes the L^{∞} norm of the function f on the domain.

24 end

Our main theoretical result in Theorem 1 demonstrates the representation capability of neural networks for the evolution of the PDE in Eq. (1) under a manifold hypothesis. Some preliminary definition about manifold is presented in Appendix A.

Theorem 1. Let \mathcal{M} be an m-dimensional compact smooth Riemannian manifold isometrically embedded in \mathbb{R}^n with reach $\tau_{\mathcal{M}} > 0$. Suppose the PDE solution of (12) is driven by a Lipschitz³

The evolutionary operator \mathfrak{F} is Lipschitz in the sense that $\|\mathfrak{F}(\boldsymbol{u}_1(\boldsymbol{x},t,\boldsymbol{\zeta}),\tau,\boldsymbol{\zeta}) - \mathfrak{F}(\boldsymbol{u}_2(\boldsymbol{x},t,\boldsymbol{\zeta}),\tau,\boldsymbol{\zeta})\| \le \text{Lip}_{\mathfrak{F}}\|\boldsymbol{u}_1(\boldsymbol{x},t,\boldsymbol{\zeta}) - \boldsymbol{u}_2(\boldsymbol{x},t,\boldsymbol{\zeta})\|$ for all $\boldsymbol{u}_1(\boldsymbol{x},t,\boldsymbol{\zeta}), \boldsymbol{u}_2(\boldsymbol{x},t,\boldsymbol{\zeta}) \in \mathcal{M}$ and all $t,\tau,\boldsymbol{\zeta}$. Here $\text{Lip}_{\mathfrak{F}}$ denotes the Lipschitz constant of \mathfrak{F} .

evolutionary operator

$$u(x, t + \tau, \zeta) = \mathfrak{F}(u(x, t, \zeta), \tau, \zeta)$$

and all solutions lie on \mathcal{M} such that $\{\boldsymbol{u}(\boldsymbol{x},t,\boldsymbol{\zeta})\}\subset\mathcal{M}\subset[-B,B]^n$ for some B>0. For any $\varepsilon\in(0,1)$, there exists an encoder ReLU ⁴ network $\mathcal{E}_{\theta_e}\in\mathcal{F}_{\mathrm{NN}}(n,C_{\mathcal{M}}(m+1),L_E,p_E,K_E,\kappa_E,M_E)$, a decoder ReLU network $\mathcal{D}_{\theta_d}\in\mathcal{F}_{\mathrm{NN}}(C_{\mathcal{M}}(m+1),n,L_D,p_D,K_D,\kappa_D,M_D)$, and a propagator ReLU network $\mathcal{P}_{\theta_d}\in\mathcal{F}_{\mathrm{NN}}(C_{\mathcal{M}}(m+1),C_{\mathcal{M}}(m+1),L_P,p_P,K_P,\kappa_P,M_P)$ with

$$L_E = O(\log \varepsilon^{-1}), \ p_E = O(\varepsilon^{-m}), \ K_E = O(\varepsilon^{-m}\log \varepsilon^{-1}), \ \kappa_E = O(\varepsilon^{-m}), \ M_E = O(1)$$

$$L_D = O(\log \varepsilon^{-1}), \ p_D = O(\varepsilon^{-m}), \ K_D = O(\varepsilon^{-m}\log \varepsilon^{-1}), \ \kappa_D = O(\varepsilon^{-m}), \ M_D = B$$

$$L_P = O(\log \varepsilon^{-1}), \ p = O(\varepsilon^{-m}), \ K = O(\varepsilon^{-m}\log \varepsilon^{-1}), \ \kappa = O(\varepsilon^{-m}) \ M_P = O(1)$$

such that

$$\left\| \mathcal{D}_{\theta_d} \circ \mathcal{P}_{\theta_p} (\mathcal{E}_{\theta_e} (\boldsymbol{u}(\boldsymbol{x}, t, \boldsymbol{\zeta}), \tau, \boldsymbol{\zeta}) - \mathfrak{F}(\boldsymbol{u}(\boldsymbol{x}, t, \boldsymbol{\zeta}), \tau, \boldsymbol{\zeta}) \right\| \le \left(\operatorname{Lip}_{\mathcal{D}_{\theta_d}} \operatorname{Lip}_{\mathcal{P}_{\theta_p}} + \operatorname{Lip}_{\mathcal{D}_{\theta_d}} + 1 \right) \varepsilon.$$
 (6)

The constants hidden in $O(\cdot)$ depend on $m, n, \tau_{\mathcal{M}}$, $B, C_{\mathcal{M}}$ (the number of charts for \mathcal{M}) and the output, derivatives of the coordinate maps ϕ_i 's of \mathcal{M} and the partition of unity ρ_i 's up to order 1. In Eq. (6), $\operatorname{Lip}_{\mathcal{D}_{\theta_d}}$ and $\operatorname{Lip}_{\mathcal{P}_{\theta_p}}$ denote the Lipschitz constants⁵ of the decoder network and the propagator network respectively.

Theorem 1 is proved in Appendix A. Theorem 1 establishes the representational capacity of neural networks within an encoder–decoder and latent-space propagator framework for approximating the evolutionary operator \mathfrak{F} . As the approximation accuracy ε varies, the network size in Theorem 1 scales in a power law of ε , and importantly, the power depends on the intrinsic dimension m instead of the data dimension n. The error in Eq. (6) is magnified by factors depending on the Lipschitz constants of the decoder network and the propagator network. For stable prediction, the decoder and the propagator networks with smaller Lipschitz constants are generally preferred.

Our propagator loss in Eq. (2) is evaluated on the difference between the true solution $\boldsymbol{u}(\boldsymbol{x},t+\tau,\boldsymbol{\zeta})$ and the predicted solution $\hat{\boldsymbol{u}}(\boldsymbol{x},t+\tau,\boldsymbol{\zeta})$, rather than in the latent space. The latent representation of the high-dimensional solution $\boldsymbol{u}(\boldsymbol{x},t+\tau,\boldsymbol{\zeta})$ is obtained by encoding it with the encoder \mathcal{E}_{θ_e} :

$$\tilde{\boldsymbol{z}}(t+\tau,\boldsymbol{\zeta}) = \mathcal{E}_{\theta_e}\left(\boldsymbol{u}(\boldsymbol{x},t+\tau,\boldsymbol{\zeta})\right).$$
 (7)

In contrast, the predicted latent representation is generated by propagating the encoded state at time t using the latent-space propagator \mathcal{P}_{θ_p} :

$$\hat{\boldsymbol{z}}(t+\tau,\boldsymbol{\zeta}) = \mathcal{P}_{\theta_n}\left(\mathcal{E}_{\theta_e}\left(\boldsymbol{u}(\boldsymbol{x},t,\boldsymbol{\zeta})\right),\tau,\boldsymbol{\zeta}\right). \tag{8}$$

When the propagator loss is evaluated in the physical space using $\|\boldsymbol{u}(\boldsymbol{x},t+\tau,\boldsymbol{\zeta}) - \hat{\boldsymbol{u}}(\boldsymbol{x},t+\tau,\boldsymbol{\zeta})\|$, rather than in the latent space using $\|\tilde{\boldsymbol{z}}(t+\tau,\boldsymbol{\zeta}) - \hat{\boldsymbol{z}}(t+\tau,\boldsymbol{\zeta})\|$, the latent vectors $\tilde{\boldsymbol{z}}$ and $\hat{\boldsymbol{z}}$ are not explicitly forced to coincide. Although both aim to represent the same physical state $\boldsymbol{u}(\boldsymbol{x},t+\tau,\boldsymbol{\zeta})$, they may occupy different regions in latent space due to their distinct generative paths, one derived from direct encoding and the other from temporal propagation.

Our Flexi-VAE framework may yield distinct but functionally equivalent latent representations

⁴The activation function is the rectified linear unit $\sigma(a) = \max\{a, 0\}$.

⁵We consider at atlas of \mathcal{M} $\{(U_i, \phi_i)\}_{i=1}^{C_{\mathcal{M}}}$ such that each ϕ_i is an orthogonal projection onto a local tangent space, as constructed in the proof of Theorem 1 in Appendix A. Denote $b = \max\left(\sup_{\boldsymbol{u}(\boldsymbol{x},t,\boldsymbol{\zeta})\in\mathcal{M}}\max_{j}\|\phi_{j}(\boldsymbol{u}(\boldsymbol{x},t,\boldsymbol{\zeta}))\|_{\infty},1\right)$. The Lipschitz constant of \mathcal{D}_{θ_d} is defined such that $\|\mathcal{D}_{\theta_d}(\boldsymbol{z}_1) - \mathcal{D}_{\theta_d}(\boldsymbol{z}_2)\| \leq \operatorname{Lip}_{\mathcal{D}_{\theta_d}}\|\boldsymbol{z}_1 - \boldsymbol{z}_2\|$ for all $\boldsymbol{z}_1,\boldsymbol{z}_2 \in [-b,b]^{C_{\mathcal{M}}(m+1)}$. The Lipschitz constant of \mathcal{P}_{θ_p} is defined such that $\|\mathcal{P}_{\theta_d}(\boldsymbol{z}_1) - \mathcal{P}_{\theta_d}(\boldsymbol{z}_2)\| \leq \operatorname{Lip}_{\mathcal{P}_{\theta_p}}\|\boldsymbol{z}_1 - \boldsymbol{z}_2\|$ for all $\boldsymbol{z}_1,\boldsymbol{z}_2 \in [-b,b]^{C_{\mathcal{M}}(m+1)}$.

for the same high-dimensional physical state. Despite this difference in the latent space, both representations yield nearly identical reconstructions when passed through the shared decoder:

$$\mathcal{D}_{\theta_d}\left(\tilde{\boldsymbol{z}}(t+\tau,\boldsymbol{\zeta})\right) \approx \mathcal{D}_{\theta_d}\left(\hat{\boldsymbol{z}}(t+\tau,\boldsymbol{\zeta})\right) \approx \boldsymbol{u}(\boldsymbol{x},t+\tau,\boldsymbol{\zeta}). \tag{9}$$

Even though $\tilde{z}(t+\tau,\zeta)$ and $\hat{z}(t+\tau,\zeta)$ may be different, the propagated latent code $\hat{z}(t+\tau,\zeta)$ tends to give rise to better stability. In Section 3.1.5, we analyze the local sensitivity the decoder at \tilde{z} and \hat{z} by computing the Jacobian $\mathbf{J} = \partial \mathcal{D}\theta_d/\partial z$ locally and performing singular value decomposition (SVD) to assess directional stretching and contraction. The decoder sensitivity, quantified by the Jacobian norm and its spectral properties, provides insight into the robustness of latent reconstructions under perturbations. Additionally, we evaluate the pullback Riemannian metric $g_z = \mathbf{J}^{\top} \mathbf{J}$ and its determinant to measure local volume distortion induced by the decoder.

Through an example of a nonlinear PDE in Section 3.1.5, we show that the latent vectors in propagated latent space (\hat{z}) typically reside in regions of lower decoder sensitivity, whereas those obtained from direct encoding (\tilde{z}) are more susceptible to amplification of perturbations. These observations highlight the role of the propagator in guiding latent trajectories toward geometrically stable regions of latent space, a property that underpins the robustness of long-horizon predictions in the Flexi-VAE framework.

3 Numerical Results

To validate the proposed framework, we evaluate its performance on two canonical benchmark problems: the one-dimensional (1D) nonlinear viscous Burgers' equation and the two-dimensional (2D) advection—diffusion equation.

3.1 1D Viscous Burgers' Equation

The 1D viscous Burgers' equation serves as a canonical benchmark for studying nonlinear wave propagation and shock formation under varying levels of viscosity [44]. It is governed by:

$$\frac{\partial u}{\partial t} + u \frac{\partial u}{\partial x} = \nu \frac{\partial^2 u}{\partial x^2},\tag{10}$$

subject to initial and boundary conditions:

$$u(x,0) = u_0(x), \quad u(0,t) = u(L,t) = 0, \quad x \in [0,L].$$

Here, u(x,t) denotes the velocity field, and ν is the kinematic viscosity. The spatial domain [0,L] with L=1 is discretized using 128 uniform grid points, resulting in a 128-dimensional state vector for each time step. The time step is fixed to $\Delta t=0.004$. We consider a smooth initial profile chosen such that a closed-form solution exists, parameterized by the Reynolds number $\text{Re}=1/\nu$. The exact solution, derived via the Cole–Hopf transformation, evolves as:

$$u(x,t) = \frac{x}{t+1+\sqrt{\frac{t+1}{t_0}}\exp\left(\frac{\operatorname{Re} x^2}{4(t+1)}\right)}, \quad \text{where } t_0 = \exp\left(\frac{\operatorname{Re}}{8}\right). \tag{11}$$

This analytical solution serves as the reference to assess the reconstruction and forecasting performance of our proposed model. The highly nonlinear nature of the Burgers' dynamics, particularly under high Re, introduces sharp gradients that challenge standard forecasting models and thus provide a rigorous testbed for evaluating model robustness [44].

We consider Reynolds numbers in the range Re \in [400, 2400] and forecast horizons $\tau/\Delta t \in$ [150, 450], corresponding to approximately 30% to 90% of the total wave propagation time across the domain. Lower values of Re yield smooth, diffusion-dominated dynamics, whereas higher values produce sharp, advection-dominated profiles. The dataset is partitioned using a 70-30 train-validation split across the joint (Re, τ) space. The validation set is further stratified into interpolation and extrapolation regimes to rigorously assess the model's ability to generalize at different parameter combinations. Additional details on dataset construction and evaluation protocols are provided in Appendix B.

3.1.1 Model Architecture

The model leverages a two-dimensional latent space, m=2, to capture the underlying dynamics of the Burgers' equation. This choice is motivated by the theoretical guarantee in Theorem 1, which ensures that neural networks can approximate high-dimensional solution manifolds that are intrinsically low-dimensional. To empirically validate this assumption, we estimate the intrinsic dimension of the dataset using the Maximum Likelihood Estimation (MLE) method with k=5,10 nearest neighbors, implemented via the scikit-dimension package [6]. The results consistently yield intrinsic dimension estimate of 1.97, supporting the use of a 2D latent space as both theoretically justified and empirically sufficient for capturing the governing dynamics in a parsimonious representation.

Temporal evolution is achieved through two distinct latent neural propagators: the Positional-Encoding Propagator (PEP), which utilizes sinusoidal embeddings for Reynolds number (Re) and temporal offsets (τ) , and the Direct Concatenation Propagator (DCP), which directly concatenates these parameters with the latent vector. Bayesian optimization is employed to fine-tune critical hyperparameters for both PEP and DCP via the hyperparameter tuning framework provided by WandB [42]. The optimized configurations for each propagator are summarized in Table 1. In addition to hyperparameters such as latent dimension and learning rate, we treat dataset tuples size as a key variable to assess model performance under varying levels of data availability. Further architecture details are provided in Appendix C.

Table 1: Summary of model configuration for the Burgers' equation.

Component	PEP	DCP
Embedding dimension (d)	64	-
Batch size (B)	256	64
Learning rate (α)	8×10^{-4}	7×10^{-4}
Number of epochs	150	100
KL-divergence weight (β)	4×10^{-5}	1.2×10^{-5}
Propagation loss weight (γ)	0.60	1.70
Dataset size	20,000	80,000

3.1.2 Model Performance

Fig. 5 illustrates the forecasting performance of the Direct Concatenation Propagator (DCP) on Burgers' equation across varying Reynolds numbers (Re) and forecast horizons (τ) . We show two representative cases: Axis 1 corresponds to low-Re (left extrapolation) and Axis 3 corresponds to high-Re (right extrapolation). Each case includes predictions at small, intermediate, and large values of τ , spanning up to hundreds of time steps. In the left extrapolation regime (Axis 1), the model is tested on Re values lower than those in the training range, resulting in smooth, diffusion-dominated solutions. Despite the absence of such low Re during training, the model accurately captures the solution trajectories for all τ values, demonstrating effective generalization to high-diffusivity regimes. In the right extrapolation regime (Axis 3), characterized by larger Re and the

emergence of advection-dominated dynamics with steep gradients, the model continues to perform well, maintaining accuracy even at large τ . These results confirm the ability of DCP-based Flexi-VAE to forecast across both smooth and sharp-gradient transport regimes, and their stability for long-horizon forecasts. The use of explicit parameter concatenation in the latent space provides a robust inductive bias, allowing the model to handle nontrivial extrapolation scenarios in both temporal and parametric dimensions.

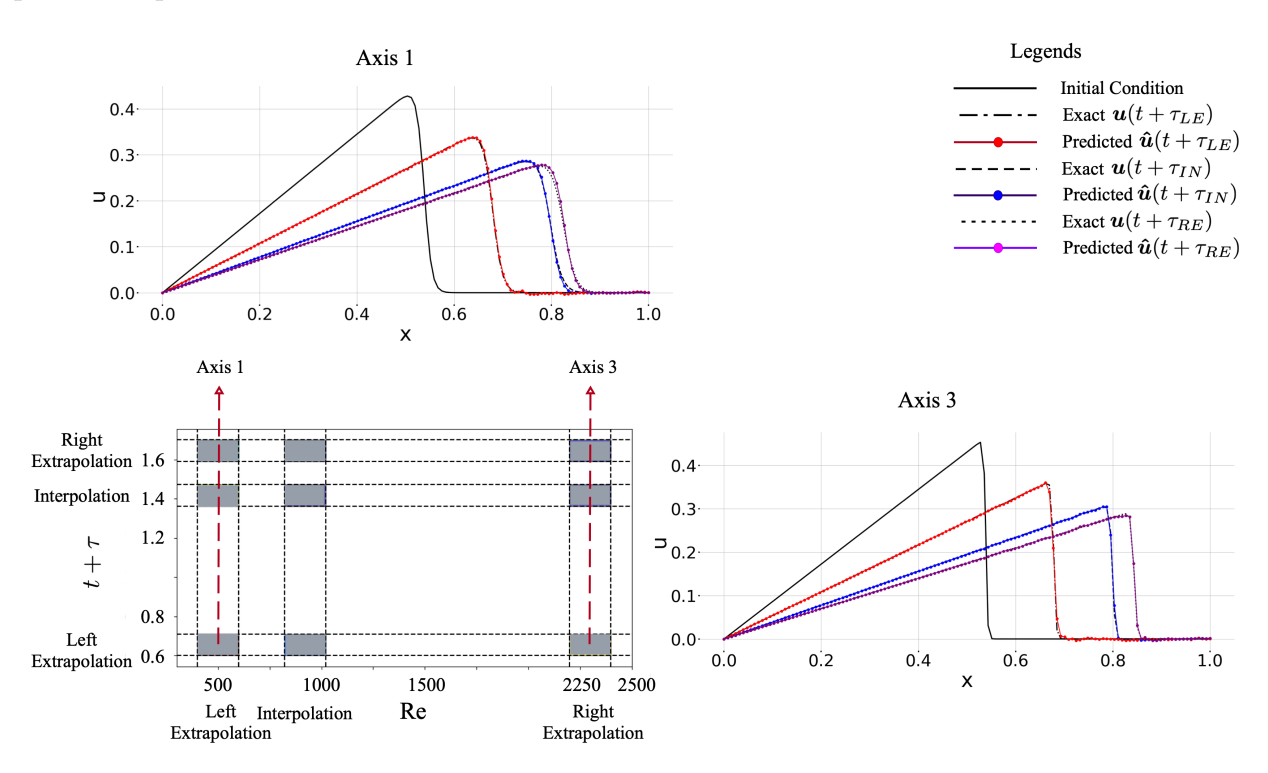


Figure 5: Forecasting performance of the DCP based Flexi-VAE model on the 1D viscous Burgers' equation across interpolation and extrapolation regimes. Bottom center: The (Re, $t+\tau$) parameter space. Axes 1 and 3 (marked in red) indicate representative slices through low and high Reynolds numbers, respectively. Top left and bottom right: Predicted and exact solutions for Axis 1 (low-Re, left extrapolation) and Axis 3 (high-Re, right extrapolation) are shown at three future time offsets: $\tau_{\rm LE}$, $\tau_{\rm IN}$, and $\tau_{\rm RE}$.

We evaluate the predictive accuracy of Flexi-VAE by computing the Mean Squared Error (MSE) over 30,000 randomly sampled initial conditions $(j=1,\ldots,J)$ and forecasting time horizon $(i=1,\ldots,I)$, shown in Fig. 6. Initial times are uniformly sampled from [0,2], and forecasts are evaluated across interpolation and extrapolation regimes. Both the Positional Encoding Propagator (PEP, Fig. 6 panel A) and the Direct Concatenation Propagator (DCP, Fig. 6 panel B) perform best in the interpolation region. However, PEP exhibits higher errors in extrapolation zones, particularly at large Re, indicating difficulty in modeling sharp gradients. In contrast, DCP maintains lower and more uniform MSE across all regions, highlighting its improved generalization. The direct parameter injection in DCP leads to a more stable latent representation under unseen (Re, τ) combinations.

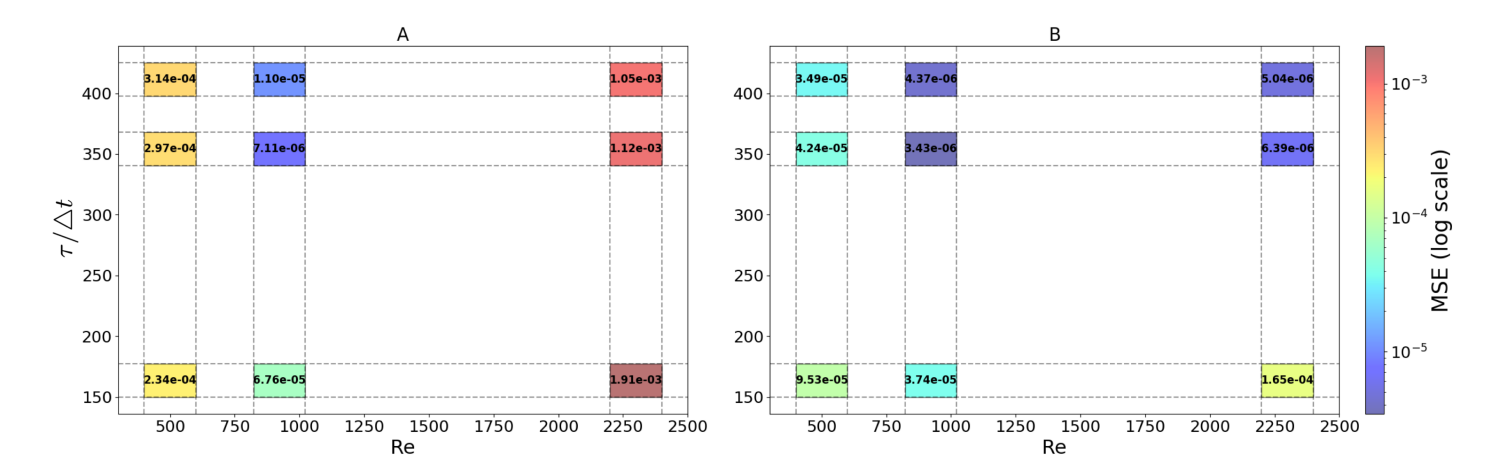


Figure 6: Mean Squared Error (MSE) distribution across 30,000 randomly sampled future state predictions for different parameter zones. The left panel (A) represents results for the Positional Encoding Propagator (PEP), while the right panel (B) corresponds to the Direct Concatenation Propagator (DCP). The heatmap showcases MSE values for left extrapolation, right extrapolation, and interpolation zones, emphasizing the model's predictive accuracy across varying combinations of Reynolds number (Re) and temporal offset (τ).

3.1.3 Comparison with other Autoencoder-based Models

We compare the prediction accuracy and computational efficiency of Flexi-VAE with a baseline Autoencoder—Long Short-Term Memory (AE-LSTM) framework. The AE-LSTM first encodes the input state into a 2D latent space using a nonlinear autoencoder, then evolves these latents using a two-layer LSTM conditioned on Reynolds number (Re), followed by decoding to reconstruct the high-dimensional state. The autoencoder and decoder architectures are designed to match the parameter count of those used in Flexi-VAE, ensuring a fair basis for comparison.

The AE-LSTM is trained on Re \in [600, 625, ..., 2225] and tested on extrapolated Re \in [550, 1025, ..., 2450], using 500 snapshots per simulation. For each test Re, predictions begin from the initial state (t_0) and are evaluated at three unseen forecast horizons $\tau/\Delta t = \{155, 345, 450\}$. Flexi-VAE performs single-shot predictions to the desired offset, whereas AE-LSTM uses a rolling forecast initialized with a 40-step input window.

Fig. 7 shows the predicted solutions at Re = 550 (left extrapolation) and Re = 2450 (right extrapolation). At Re = 550, Flexi-VAE closely matches the exact solution across all τ , while AE-LSTM shows increasing error at large τ due to compounding errors in its autoregressive formulation. At Re = 2450, both models perform well at small τ , but AE-LSTM again exhibits drift at longer forecast horizons. These results demonstrate the stability advantage of Flexi-VAE's single-step forecasting, particularly under extrapolation.

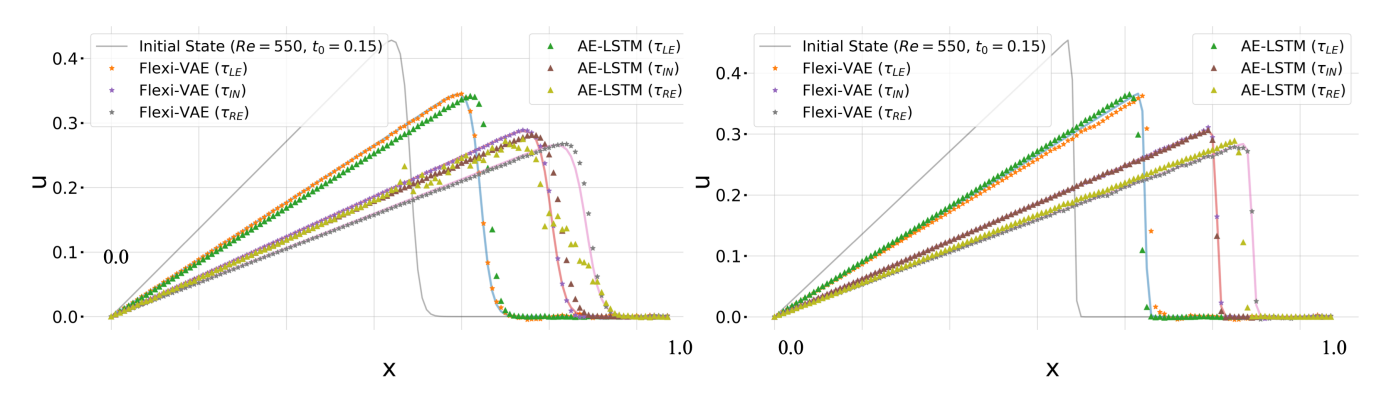


Figure 7: Temporal evolution analysis for left and right extrapolation Reynolds numbers. Predictions are evaluated at $\tau = [155, 345, 450]$. The plots showcase the exact solution (solid lines), Flexi-VAE predictions (circle symbols), and AE-LSTM predictions (triangle symbols) across all cases.

We also assess runtime performance for both models across varying τ values. Each benchmark is

repeated over 300 trials on both CPU and GPU to ensure statistical reliability. As shown in Fig. 8, AE-LSTM runtime increases linearly with τ due to its $\mathcal{O}(n)$ sequential nature. In contrast, Flexi-VAE achieves constant $\mathcal{O}(1)$ runtime, completing predictions in ~ 0.004 s on CPU and ~ 0.0006 s on GPU regardless of τ . For large offsets, Flexi-VAE offers speedups of up to 50x on CPU and 90x on GPU. All benchmarks are performed on an Intel Core i9-13900K CPU (32 threads) and an NVIDIA GeForce RTX 3090 GPU (24 GB VRAM). This efficiency makes Flexi-VAE well-suited for real-time and long-horizon forecasting tasks where latency and scalability are critical.

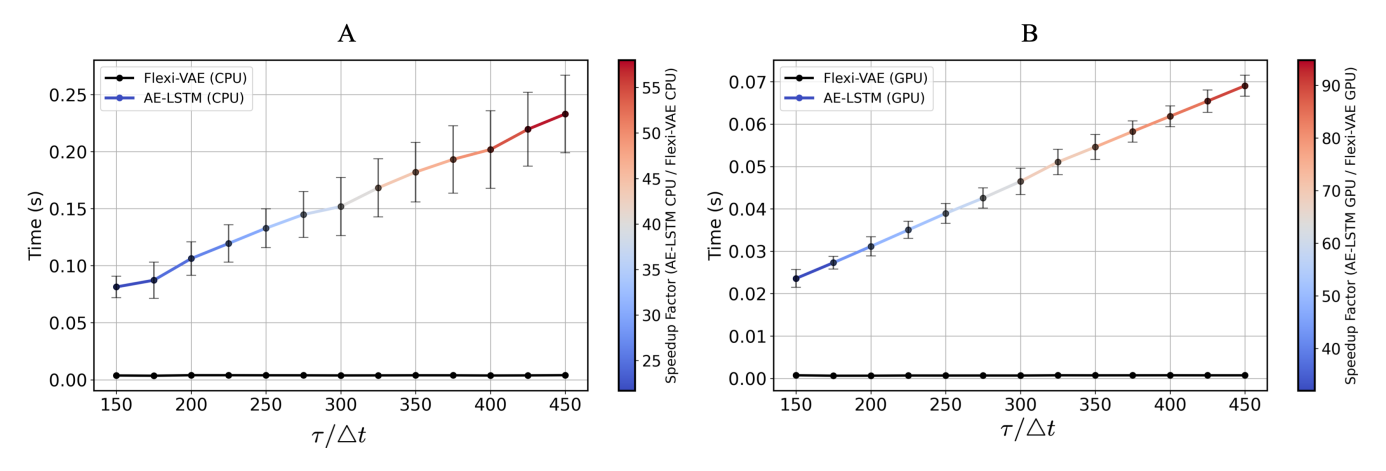


Figure 8: Prediction time comparison for Flexi-VAE and AE-LSTM across a range of temporal offsets (τ) on CPU and GPU. The AE-LSTM model exhibits a linear increase in execution time with τ due to its autoregressive nature $(\mathcal{O}(n))$, while Flexi-VAE maintains constant execution time $(\mathcal{O}(1))$ across all τ values. Flexi-VAE achieves up to a 50x speedup on CPU and a 90x speedup on GPU compared to AE-LSTM, demonstrating superior computational efficiency and scalability.

3.1.4 Model Scalability, Data Efficiency and Physical Interpretability

Disentangled latent representations are crucial for generalization in dynamical systems modeling [4, 17]. We assess the influence of propagator architecture on scalability, data efficiency, and physical interpretability by comparing the PEP and DCP designs. Both models are trained on datasets with varying sample sizes and evaluated in extrapolation regimes where Re and τ lie outside the training range. As shown in Fig. 9, DCP achieves stable performance with as few as 80K samples, while PEP exhibits non-monotonic error trends, indicating poor generalization.

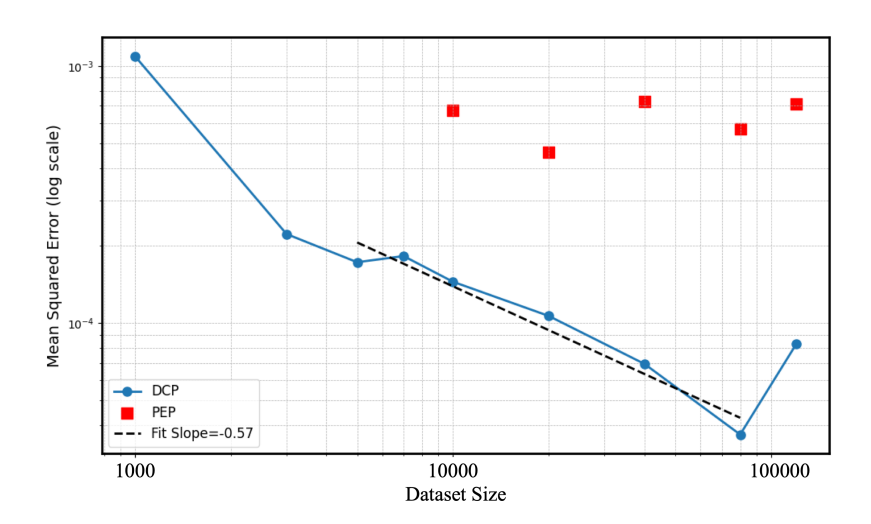


Figure 9: Mean squared error (MSE) on the Reynolds number extrapolation region as a function of dataset size (number of training tuples, log-log scale). The Direct Concatenation Propagator (DCP) exhibits consistent improvement with increasing data, achieving a minimum MSE near 80K samples and following a power-law scaling with slope -0.57. In contrast, the Positional Encoding Propagator (PEP) displays non-monotonic and unstable behavior, indicating poor generalization in data-sparse regimes.

We quantify data efficiency by examining the decay of MSE with increasing dataset tuple size in log-log scale in Fig. 9. For DCP, the validation MSE exhibits a power-law decay with respect to

dataset size in the range of 7K to 80K, appearing approximately linear when plotted on a log-log scale. A least-squares fit over this range yields a slope of -0.57, corresponding to the empirical scaling law MSE $\sim p^{-0.57}$, where p denotes the number of dataset tuples used for training. PEP shows inconsistent behavior and lacks a clear decay trend, further confirming its poor generalization in extrapolation settings.

To analyze the latent structure, we decode a uniform grid of points in the latent space to generate physical fields. From these fields, we extract two key quantities: sharpness (max $|\partial u/\partial x|$), which reflects the influence of the Reynolds number (Re), and peak position, which is primarily governed by advection over time t. Fig. 10 compares the latent space organization of PEP and DCP across increasing training dataset sizes, where each size refers to the number of dataset tuples used for training. The DCP model produces a smooth and well-structured latent space, with \hat{z}_1 consistently encoding peak position and \hat{z}_2 encoding sharpness. This disentangled representation becomes increasingly pronounced as the dataset size grows, indicating stable generalization and meaningful compression of physical features. In contrast, PEP exhibits entangled and irregular latent structures, particularly at smaller training sizes, where distortions and discontinuities are evident. This irregularity suggests that PEP is more susceptible to overfitting and less capable of capturing clean feature representations [3]. This contrast highlights a key advantage of the DCP architecture: its design facilitates the emergence of physically interpretable latent dimensions by leveraging forecasting objectives to shape the representation space. In PEP, the higher-dimensional latent space lacks such structure, making it harder for the model to consistently associate latent directions with physical phenomena, especially under limited data regimes.

Unlike methods such as SD-VAE [17], which rely on labeled supervision to enforce interpretability, our framework achieves disentanglement in an unsupervised setting through architectural design and regularization. This enables applicability to real-world PDE systems where governing parameters are unknown or hard to measure.

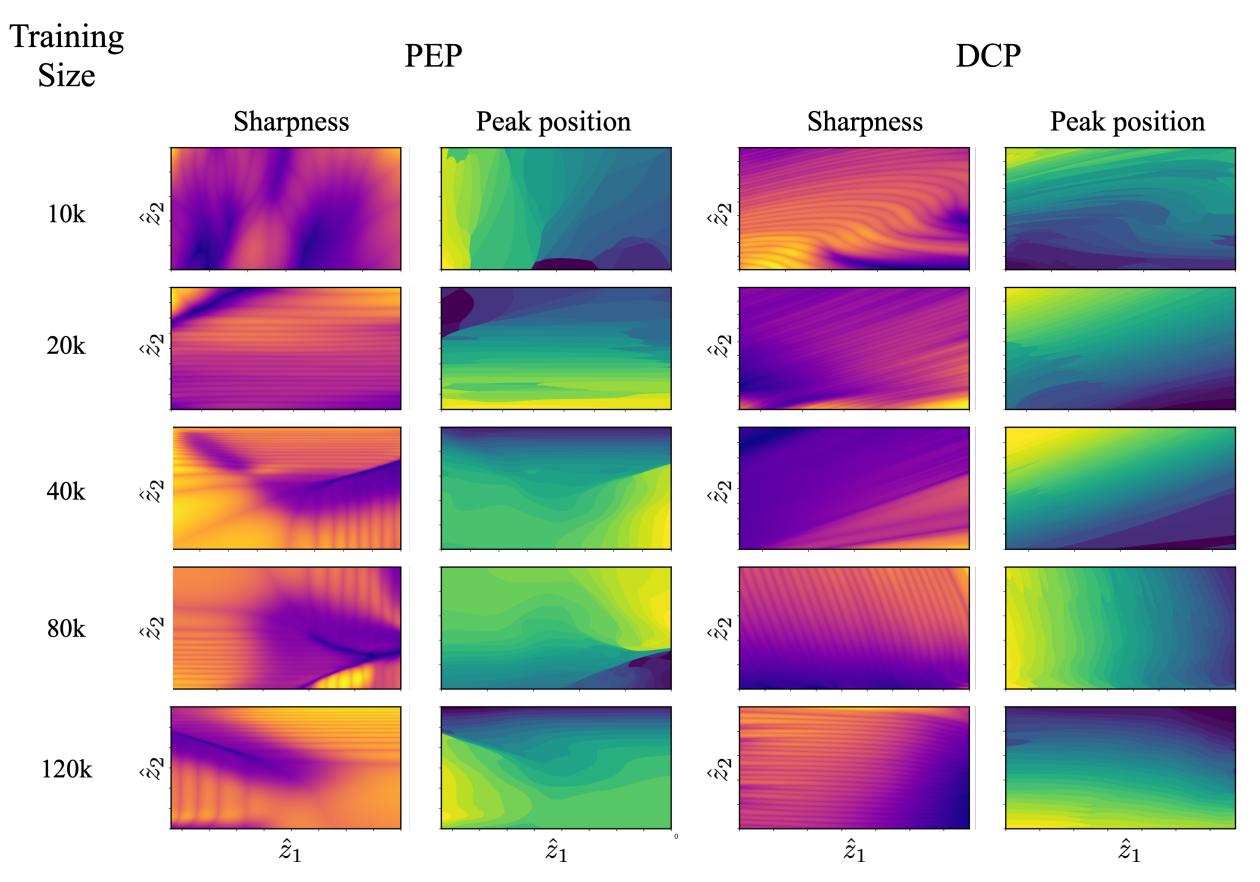


Figure 10: Latent space structure for PEP (left) and DCP (right) across training sizes. Each point in the latent space is decoded into a high-dimensional field, from which sharpness (max $|\partial u/\partial x|$) and peak position are extracted. The DCP architecture results in a structured latent space where \hat{z}_1 corresponds to peak position and \hat{z}_2 corresponds to sharpness. In contrast, PEP exhibits entangled representations in which these physical attributes do not separate cleanly.

3.1.5 Geometric Analysis

We analyze the local behavior of the decoder \mathcal{D}_{θ_d} at two latent vectors that produce nearly identical reconstructions: the original latent vector $\tilde{\boldsymbol{z}}(t_0+\tau,\boldsymbol{\zeta})$, obtained by encoding the ground truth at the future time, and the propagated latent vector $\hat{\boldsymbol{z}}(t_0+\tau,\boldsymbol{\zeta})$, generated by advancing the initial latent state through the learned propagator. Although both map to nearly the same high-dimensional field,

$$\mathcal{D}_{\theta_d}(\tilde{oldsymbol{z}}) pprox \mathcal{D}_{\theta_d}(\hat{oldsymbol{z}}),$$

they reside in geometrically distinct regions of the latent space.

Let $\mathbf{J}(\mathbf{z}) = \partial \mathcal{D}_{\theta_d}(\mathbf{z}(t, \boldsymbol{\zeta}))/\partial \mathbf{z} \in \mathbb{R}^{n \times m}$ denote the Jacobian of the decoder, capturing how infinitesimal perturbations in the 2D latent space affect the reconstructed 128-dimensional PDE solution. We compute \mathbf{J} at both $\tilde{\mathbf{z}}$ and $\hat{\mathbf{z}}$, where both latent codes produce nearly identical outputs under the same trained decoder. To probe how local perturbations influence specific regions of the reconstructed field, we color the signal according to the magnitude of the first column of \mathbf{J} —i.e., the decoder sensitivity with respect to the first latent coordinate. This visualization reveals the spatial regions in the output that are most sensitive to variations in latent space. Although both latents yield visually indistinguishable outputs, the decoder response around $\tilde{\mathbf{z}}$ is more concentrated and anisotropic near the shock-like region, whereas the response around $\hat{\mathbf{z}}$ is more uniformly distributed across the domain as shown in Fig. 11.

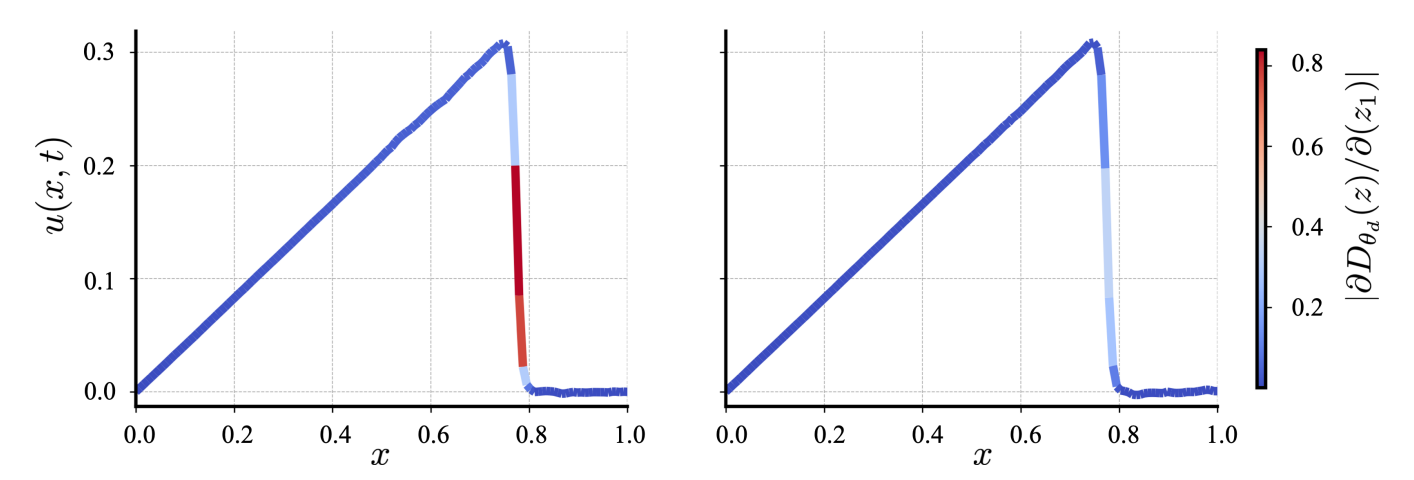


Figure 11: High-dimensional reconstructions of $\boldsymbol{u}(\boldsymbol{x},t,\boldsymbol{\zeta})$ obtained by decoding (left) $\tilde{\boldsymbol{z}}$ and (right) $\hat{\boldsymbol{z}}$, each colorcoded by the magnitude of the Jacobian $|\partial \mathcal{D}_{\theta_d}/\partial z_1|$ at that point. Despite yielding nearly identical outputs, the decoder exhibits sharper sensitivity at $\tilde{\boldsymbol{z}}$, particularly near the shock, indicating anisotropic geometry in latent space.

To evaluate decoder robustness, we apply small perturbations ϵ along each latent dimension, forming $\mathbf{z}_{\epsilon}^{(j)} = \mathbf{z} + \epsilon \mathbf{e}_{j}$. The perturbed reconstructions, shown in Fig. 12, reveal that $\tilde{\mathbf{z}}$ induces strong variations in the output field, particularly near shock fronts, while $\hat{\mathbf{z}}$ yields more stable reconstructions, reflecting a flatter local geometry.

We further analyze the decoder's local geometry via singular value decomposition (SVD) of **J**:

$$\mathbf{J} = \mathbf{U} \Sigma \mathbf{V}^{\mathsf{T}}, \quad \Sigma = \mathrm{diag}(\sigma_1, \dots, \sigma_m).$$

At \tilde{z} , the singular value spectrum σ_j of the decoder Jacobian is broader and exhibits higher magnitudes, indicating anisotropic scaling and greater sensitivity to perturbations. In contrast, the spectrum at \hat{z} is more compact, suggesting improved conditioning and local stability. As shown in Fig. 13 (middle), the Frobenius norm $\|\mathbf{J}\|_F = \sqrt{\sum_j \sigma_j^2}$ is substantially lower at \hat{z} , further confirming that the decoder exhibits more stable behavior in this region of the latent space

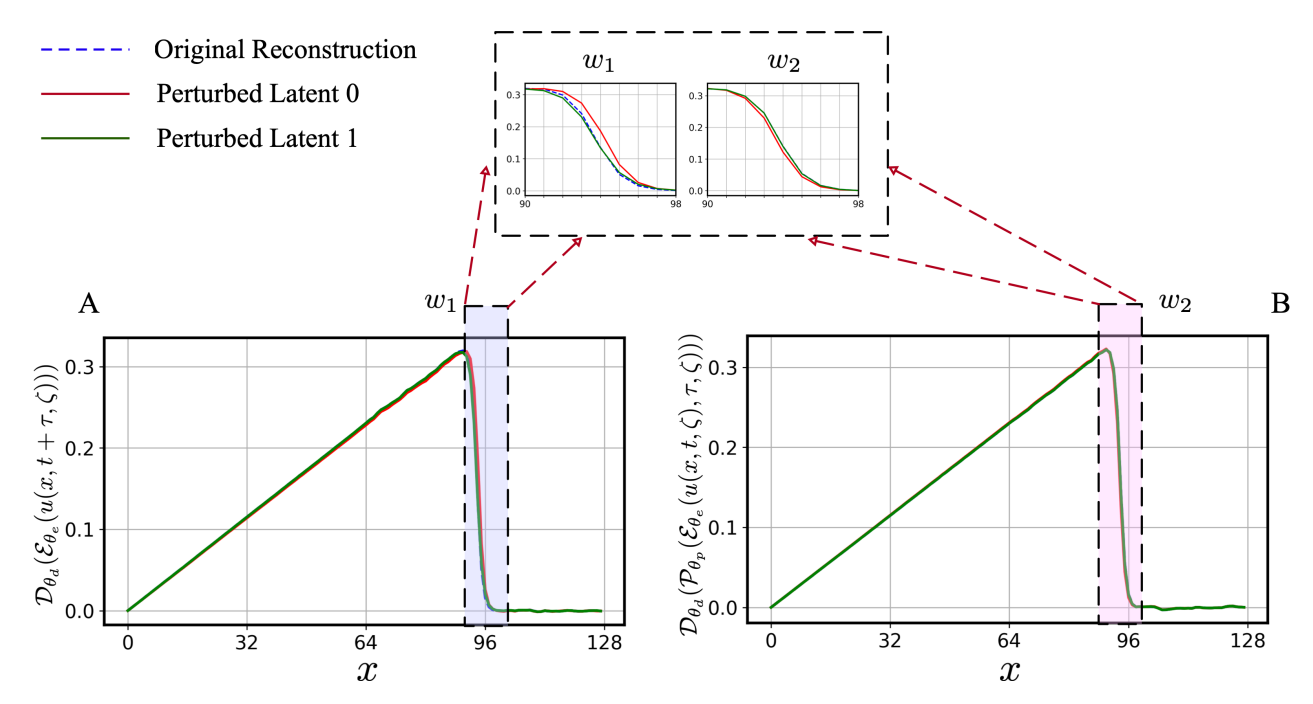


Figure 12: Effect of perturbations applied independently along each latent coordinate for the direct latent representation and the propagated representations. Panel (A): reconstructions from $\mathcal{D}_{\theta_d}(\tilde{z})$ and its perturbed versions $\mathcal{D}_{\theta_d}(\tilde{z} + \epsilon e_1)$ and $\mathcal{D}_{\theta_d}(\tilde{z} + \epsilon e_2)$. Panel (B): reconstructions from $\mathcal{D}_{\theta_d}(\hat{z})$ and its perturbed versions $\mathcal{D}_{\theta_d}(\hat{z} + \epsilon e_1)$ and $\mathcal{D}_{\theta_d}(\hat{z} + \epsilon e_2)$. Insets w_1 and w_2 magnify the regions of maximal sensitivity near the shock front, highlighting the differing responses to perturbations in the direct and propagated representations.

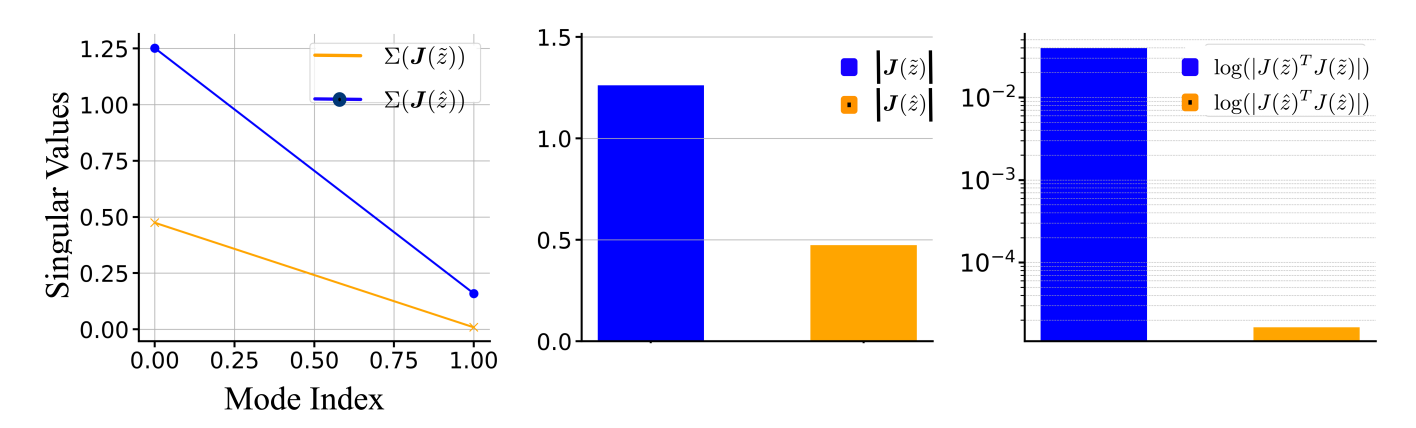


Figure 13: From left to right: (**Left**) Singular value spectra $\Sigma(\mathbf{J}(\tilde{z}))$ and $\Sigma(\mathbf{J}(\hat{z}))$, illustrating the principal local scaling behavior of the decoder at direct and propagated representations. (**Middle**) Frobenius norms $\|\mathbf{J}(\tilde{z})\|_F$ and $\|\mathbf{J}(\hat{z})\|_F$, providing an aggregate measure of decoder sensitivity. (**Right**) Comparison of log (det($\mathbf{J}^{\mathsf{T}}\mathbf{J}$)) at the direct and propagated representations. A larger determinant at \tilde{z} indicates greater local volume expansion and sensitivity, while the smaller determinant at \hat{z} reflects reduced distortion and enhanced stability.

To quantify geometric distortion, we compute the determinant of the pullback Riemannian metric $\mathbf{J}^{\mathsf{T}}\mathbf{J}$:

$$\det(\mathbf{J}^{\top}\mathbf{J}) = \prod_{i} \sigma_{j}^{2},$$

which reflects local volume expansion in the latent-to-physical map. As shown in Fig. 13 (right), this quantity is two orders of magnitude larger at \tilde{z} than at \hat{z} , indicating that direct concatenation space lies in a more sensitive, less robust region of latent space.

Although \tilde{z} and \hat{z} reconstruct to similar high-dimensional outputs, their neighborhoods differ markedly in geometry. The propagated latent \hat{z} resides in a region where the decoder is smoother and more stable. This indicates that the learned propagator \mathcal{P}_{θ_p} steers latent trajectories toward geometrically favorable regions, promoting robustness and long-term stability. These results highlight a key advantage of Flexi-VAE's architecture: the model regularizes its predictions to occupy well-conditioned regions of latent space, improving reliability in forecasting tasks.

3.2 2D Advection–Diffusion

The 2D advection–diffusion equation models the transport of a scalar field u(x, y, t) (e.g., temperature or concentration) under the combined influence of advection and isotropic diffusion:

$$\frac{\partial u}{\partial t} + c \frac{\partial u}{\partial x} = \nu \left(\frac{\partial^2 u}{\partial x^2} + \frac{\partial^2 u}{\partial y^2} \right), \tag{12}$$

where c is the constant advection velocity in the x-direction and $\nu = 1/\alpha$ is the diffusion coefficient. The left-hand side captures temporal change and directional transport, while the right-hand side represents spatial spreading due to diffusion.

Assuming an initial point-source (Dirac delta) at the origin,

$$u(x, y, 0) = \delta(x, y), \tag{13}$$

and neglecting boundary effects (i.e., infinite domain), the closed-form analytical solution is:

$$u(x, y, t) = \frac{1}{4\pi\nu t} \exp\left(-\frac{(x - ct)^2 + y^2}{4\nu t}\right), \quad t > 0.$$
 (14)

This solution describes a Gaussian profile advected along the x-axis at speed c, while undergoing symmetric spreading in both spatial directions. Fig. 14 illustrates this combined behavior, showing downstream translation due to advection and radial spreading due to diffusion.

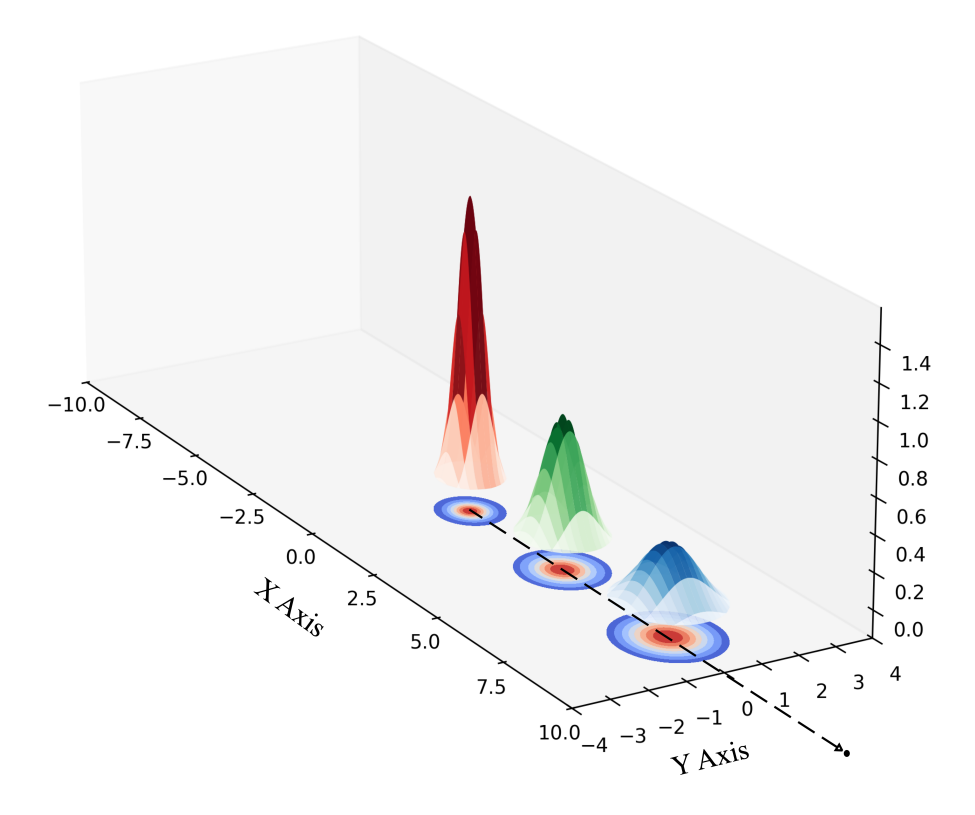


Figure 14: Schematic representation of the advection-diffusion process. The scalar field is transported in the x-direction at a constant velocity c while undergoing isotropic diffusion in the xy-plane.

While the analytical solution is used here to generate reference data, the Flexi-VAE model does not require access to it. Instead, it operates solely on observed system trajectories and associated

parameters.

For this problem, we fix the advection velocity at c=1 and simulate solutions on a 128×128 uniform grid with a domain of $-2 \le x \le 2$ and $-2 \le y \le 2$. The forecast horizon $\tau/\Delta t$ is sampled from [150, 425], with a time step of $\Delta t = 0.004$. The Reynolds number, defined as $Re = 1/\nu$, is varied in the range [1, 10], covering dynamics from diffusion-dominated to advection-dominated regimes.

The dataset follows the same extrapolative validation strategy as in the Burgers' equation case, allowing us to evaluate the model's ability to generalize to unseen combinations of physical and temporal parameters.

3.2.1 Model Architecture

Building on the insights from the Burgers' equation experiments, we adopt only the Direct Concatenation Propagator (DCP) for the advection–diffusion case, as it consistently outperformed the Positional Encoding Propagator (PEP) in generalization to unseen parameters and long-horizon predictions. The DCP architecture directly concatenates the Reynolds number (Re) and temporal offset (τ) with the latent representation, enabling structured conditioning on both parametric and temporal information.

A latent space dimension of m=3 is chosen to capture the essential generative structure of the advection–diffusion system. This reflects the increased spatial complexity introduced by the second spatial dimension compared to the 1D Burgers' equation, while preserving model parsimony. To justify this choice, we estimate the intrinsic dimensionality of the dataset using the Maximum Likelihood Estimation (MLE) method with k=5 and k=10 nearest neighbors, as implemented in the scikit-dimension package [6]. The resulting intrinsic dimension estimate is approximately 2.2, supporting the selection of a 3D latent space.

Bayesian optimization is used to tune key hyperparameters, balancing reconstruction fidelity and long-horizon stability. The final configuration, summarized in Table 2, reflects the optimal tradeoff between model complexity and performance. The model is trained on 80,000 tuples, and performance is evaluated using L_2 -norm error for both reconstruction and forecasting, following the same methodology as the Burgers' experiments.

Table 2: Summary of the	he model configuration	for the Advection-Diffi	usion equation.
-------------------------	------------------------	-------------------------	-----------------

Component	\mathbf{DCP}
Latent dimension (m)	3
Batch size (B)	64
Learning rate (α)	7.0×10^{-4}
Number of epochs	75
KL-divergence weight (β)	1.152×10^{-5}
Propagation loss weight (γ)	1.15
Dataset size	80,000

3.2.2 Model Performance

Fig. 15 illustrates the model's performance for the 2D advection–diffusion equation. The bottom-left panel shows the dataset partitioning, delineating interpolation and extrapolation regions in the joint (Re, τ) space. The remaining panels present predictions along three representative axes: Axis 1 tests temporal evolution at low Re (diffusion-dominated regime), Axis 2 evaluates interpolation in Re, and Axis 3 assesses extrapolation at high Re. In each case, ground truth solutions are shown in the top row and model predictions in the bottom row.

In the left extrapolation regime (Axis 1), the model accurately captures the broad, isotropic spreading of the scalar field at low Re, despite never having encountered such high-diffusivity

conditions during training. In the interpolation regime (Axis 2), where Re and τ fall within the training distribution, the predictions are nearly indistinguishable from the ground truth, validating the fidelity of the learned latent space.

In the right extrapolation regime (Axis 3), characterized by higher Re and sharper advection-dominated gradients, the model retains high predictive accuracy across increasing τ , reconstructing key transport structures despite the reduced diffusion. These results highlight the model's robustness across varying dynamical regimes and forecasting horizons.

The strong performance across all axes reflects the effectiveness of the Direct Concatenation Propagator (DCP) in embedding physical parameters within the latent space, enabling generalization across both smooth (diffusive) and sharp (advective) transport regimes.

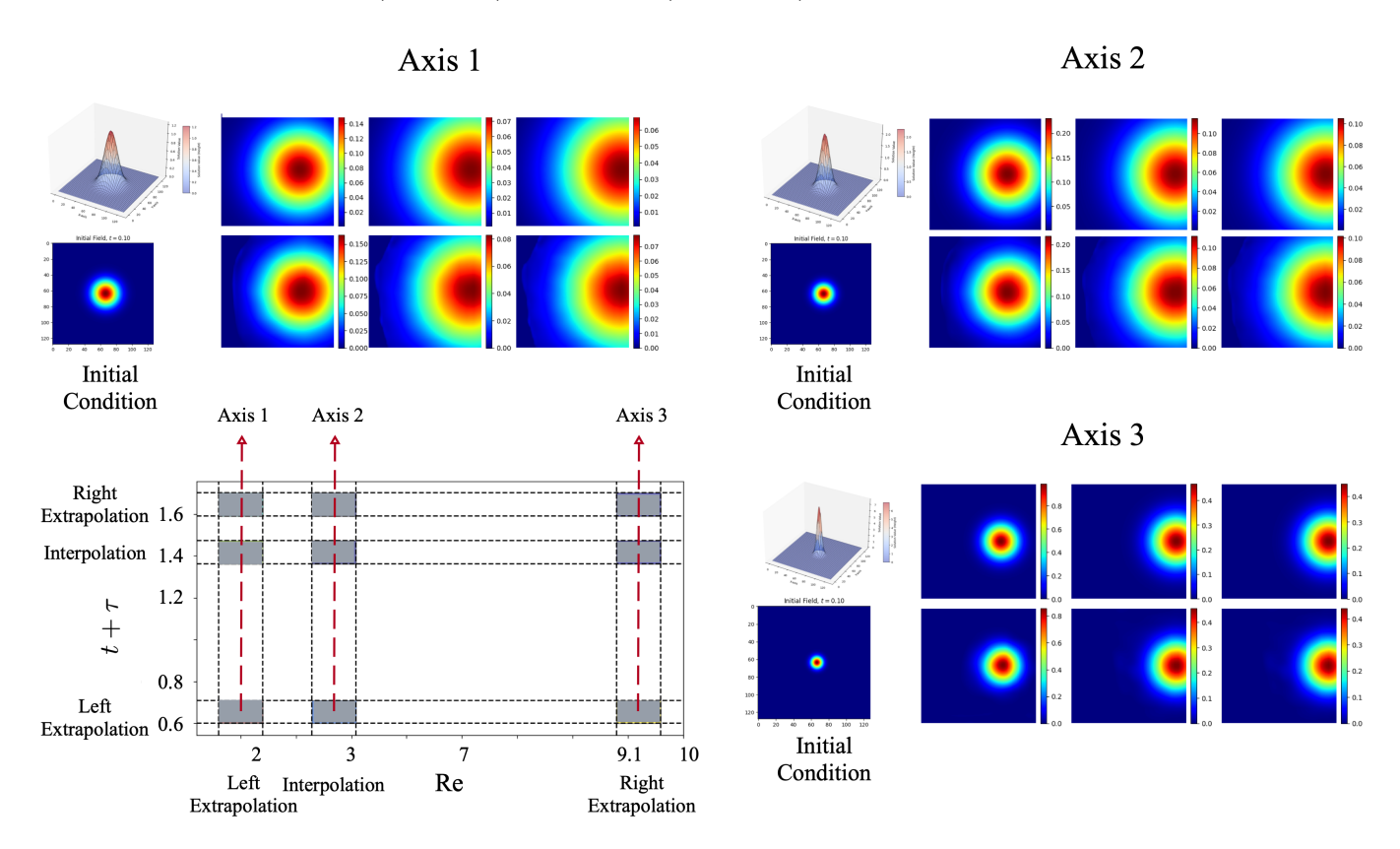


Figure 15: Model generalization across temporal and parametric regimes. The bottom-left panel illustrates the dataset partitioning into extrapolation and interpolation zones. Predictions are presented along three axes: Axis 1 (temporal evolution for low-Re), Axis 2 (Re interpolation), and Axis 3 (Re extrapolation). In all cases, the model effectively forecasts the evolution of the 2D advection-diffusion equation across unseen parameter combinations, capturing both diffusive and advection-dominated behaviors.

4 Concluding Remarks and Future Work

In this work, we proposed Flexi-VAE, a flexible variational autoencoder framework for efficient, single-shot forecasting of parametric partial differential equations. Our model advances latent representations in a non-recurrent manner using a feedforward parametric propagator. This design enables fast, long-horizon predictions across a wide range of parameter and temporal regimes while maintaining high fidelity in the reconstructed physical states.

We introduced and compared two latent propagator architectures: the *Positional Encoding Propagator* (PEP), which embeds parameters into a structured high-dimensional space, and the *Direct Concatenation Propagator* (DCP), which directly appends physical parameters to the latent state. Through experiments on two benchmark PDEs—the 1D nonlinear viscous Burgers' equation and the 2D advection—diffusion equation, we demonstrated that the DCP architecture consistently outperforms PEP in terms of forecasting accuracy, generalization to unseen parameters, and latent

space interpretability. Our geometric analysis further revealed that the latent representations generated via the learned propagator tend to occupy regions of latent space where the decoder is more stable and well-conditioned, contributing to robust long-horizon predictions.

Flexi-VAE also achieves significant computational gains compared to traditional sequential models such as AE-LSTM, offering up to 90× speedups on GPU with constant-time complexity across all forecast horizons. Moreover, the model learns disentangled latent representations without requiring supervision from labeled physical parameters, making it broadly applicable to systems where such quantities are unknown or partially observed.

While Flexi-VAE leverages effective and efficient data-driven techniques, its current formulation does not impose explicit physical constraints on the latent dynamics. Future extensions could incorporate *physics-informed latent propagators* that encode conservation laws or symmetries, for example, by enforcing unitary or symplectic structure in the propagator to preserve energy or phase volume. This could enhance both interpretability and extrapolation performance. Additionally, future work may explore extensions to stochastic systems, high-dimensional turbulent flows, and multi-parameter PDEs where Flexi-VAE's flexibility and speed offer promising advantages.

This work provides a scalable framework for learning dynamics of complex physical systems directly in latent space, bridging deep generative modeling with scientific forecasting. We believe that Flexi-VAE opens new avenues for integrating domain knowledge and geometric insight into the next generation of machine-learned surrogate models for PDEs.

Acknowledgments

We gratefully acknowledge Professor Alireza Tavakkoli from the Department of Computer Science and Engineering at the University of Nevada, Reno, for his support and guidance. We also thank Shariq Farooq Bhat from the Department of Computer Science at KAUST for his insightful discussions and constructive critiques, which were instrumental in shaping this work. AGN acknowledges support from the National Science Foundation AI Institute in Dynamic Systems (Award No. 2112085, Program Manager: Dr. Shahab Shojaei-Zadeh).

A Proof of Theorem 1

This section is devoted to the proof of Theorem 1. We first introduce some preliminary definition and notation in Section A.1 and then prove Theorem 1 in Section A.2.

A.1 Preliminary definition and notation

Let \mathcal{M} be a m-dimensional compact smooth Riemannian manifold isometrically embedded in \mathbb{R}^n . We next introduction some definitions which can be found in [65] and [34].

Definition 1 (Chart). A chart for \mathcal{M} is a pair (U, ϕ) such that $U \subset \mathcal{M}$ is open and $\phi : U \mapsto \mathbb{R}^m$, where ϕ is a homeomorphism (i.e., bijective, ϕ and ϕ^{-1} are both continuous).

The open set U is called a coordinate neighborhood, and ϕ is called a coordinate map on U. A chart defines a local coordinate system on \mathcal{M} . We say two charts (U,ϕ) and (V,ψ) on \mathcal{M} are C^k compatible if and only if the transition functions, $\phi \circ \psi^{-1} : \psi(U \cap V) \mapsto \phi(U \cap V)$ and $\psi \circ \phi^{-1} : \phi(U \cap V) \mapsto \psi(U \cap V)$ are both C^k . We next give the definition of an atlas.

Definition 2 (C^k Atlas). A C^k atlas for \mathcal{M} is a collection $\{(U_\alpha, \phi_\alpha)\}_{\alpha \in \mathcal{A}}$ of pairwise C^k compatible charts such that $\bigcup_{\alpha \in \mathcal{A}} U_\alpha = \mathcal{M}$.

Definition 3 (Smooth Manifold). A smooth manifold is a manifold \mathcal{M} together with a C^{∞} atlas.

The existence of an atlas on \mathcal{M} allows us to define differentiable functions.

Definition 4 (C^k Functions on \mathcal{M}). Let \mathcal{M} be a m-dimensional smooth manifold isometrically embedded in \mathbb{R}^n . A function $f: \mathcal{M} \to \mathbb{R}$ is C^k for an atlas $\{U_\alpha, \phi_\alpha\}_{\alpha \in \mathcal{A}}$, if for any α , the composition $f \circ \phi_\alpha^{-1} : \phi(U_\alpha) \to \mathbb{R}$ is continuously differentiable up to order k.

We next introduce the partition of unity, which plays a crucial role in our construction of encoder and decoder.

Definition 5 (Partition of Unity). A C^{∞} partition of unity on a manifold \mathcal{M} is a collection of non-negative C^{∞} functions $\rho_{\alpha}: \mathcal{M} \mapsto [0, \infty)$ for $\alpha \in \mathcal{A}$ such that 1). the collection of supports, $\{supp(\rho_{\alpha})\}_{\alpha \in \mathcal{A}}$ is locally finite⁶; 2). $\sum \rho_{\alpha} = 1$.

For a smooth manifold, a C^{∞} partition of unity always exists.

Proposition 1 (Existence of a C^{∞} partition of unity). Let $\{U_{\alpha}\}_{{\alpha}\in\mathcal{A}}$ be an open cover of a smooth manifold \mathcal{M} . Then there is a C^{∞} partition of unity $\{\rho_i\}_{i=1}^{\infty}$ with every ρ_i having a compact support such that $supp(\rho_i) \subset U_{\alpha}$ for some $\alpha \in \mathcal{A}$.

To characterize the curvature of a manifold, we adopt the reach of manifold introduced by Federer in [16].

Definition 6 (Reach, Definition 2.1 in [1]). Denote $C(\mathcal{M}) = \{ \boldsymbol{x} \in \mathbb{R}^n : \exists \boldsymbol{p} \neq \boldsymbol{q} \in \mathcal{M}, \|\boldsymbol{p} - \boldsymbol{x}\|_2 = \|\boldsymbol{q} - \boldsymbol{x}\|_2 = \inf_{\boldsymbol{y} \in \mathcal{M}} \|\boldsymbol{y} - \boldsymbol{x}\|_2 \}$ as the set of points that have at least two nearest neighbors on \mathcal{M} . Then the reach $\tau_{\mathcal{M}}$ is defined as $\tau_{\mathcal{M}} := \inf_{\boldsymbol{x} \in \mathcal{M}, \boldsymbol{y} \in C(\mathcal{M})} \|\boldsymbol{x} - \boldsymbol{y}\|_2$.

Reach has a straightforward geometrical interpretation: At each point $x \in \mathcal{M}$, the radius of the osculating circle is no less than $\tau_{\mathcal{M}}$. Reach determines a proper choice of an atlas for \mathcal{M} . In Section A.2, we choose each chart U_{α} contained in a ball of radius less than $\tau_{\mathcal{M}}/4$.

Definition 7 (Lipschitz function). An operator $f: \mathcal{X} \to \mathcal{Y}$ is L-Lipschitz if for all $u, v \in \mathcal{X}$, $||f(u) - f(v)||_{\mathcal{Y}} \le L||u - v||_{\mathcal{X}}$, where $||\cdot||_{\mathcal{X}}$ and $||\cdot||_{\mathcal{Y}}$ stand for the metric in \mathcal{X} and \mathcal{Y} respectively.

Notation. We introduce some notation to be used in the proof of Theorem 1. For a function $f: \Omega \to \mathbb{R}$, we denote its L^{∞} norm by $||f||_{L^{\infty}(\Omega)} := \sup_{\boldsymbol{x} \in \Omega} |f(\boldsymbol{x})|$. For two functions f and g, we use $f \circ g$ to denote their composition.

A.2 Proof of Theorem 1

Theorem 1 is proved in a geometric encoder-decoder representation framework for the manifold \mathcal{M} with neural network approximation theories in [70, 8].

• A geometric encoder-decoder representation framework. We first present a geometric encoder-decoder representation framework for the manifold \mathcal{M} , following [8, Theorem 1] and [38, Lemma 4] and their proofs. We claim that, for the manifold \mathcal{M} in Theorem 1, there exist an oracle encoder and decoder pair $\mathcal{E}^* : \mathcal{M} \to \mathbb{R}^{C_{\mathcal{M}}(m+1)}$ and $\mathcal{D}^* : \mathbb{R}^{C_{\mathcal{M}}(m+1)} \to \mathcal{M}$ satisfying

$$\mathcal{D}^* \circ \mathcal{E}^*(\boldsymbol{u}) = \boldsymbol{u}, \ \forall \boldsymbol{u} \in \mathcal{M}. \tag{15}$$

Here $C_{\mathcal{M}}$ denotes the number of charts for \mathcal{M} . We call \mathcal{E}^* and \mathcal{D}^* as the oracle encoder and decoder for the manifold \mathcal{M} . These oracles are constructed in the proof of [8, Theorem 1] and [38, Lemma 4], but we still present its construction for completeness. The construction of \mathcal{E}^* and \mathcal{D}^* relies on a

⁶A collection $\{A_{\alpha}\}$ is locally finite if every point has a neighborhood that meets only finitely many of A_{α} 's.

proper construction of an atlas of \mathcal{M} and a partition of unity of \mathcal{M} . We construct \mathcal{E}^* and \mathcal{D}^* using the following two steps.

Step 1. Construction of an atlas. Denote the open Euclidean ball with center c and radius r in \mathbb{R}^n by $\mathcal{B}(\boldsymbol{c},r)$. For any r>0, the collection $\{\mathcal{B}(\boldsymbol{c},r)\}_{\boldsymbol{c}\in\mathcal{M}}$ is an open cover of \mathcal{M} . Since \mathcal{M} is compact, there exists a finite collection of points c_i for $i = 1, ..., C_M$ such that $\mathcal{M} \subset \bigcup_i \mathcal{B}(c_i, r)$.

We pick the radius $r < \tau_{\mathcal{M}}/4$ so that $U_i = \mathcal{M} \cap \mathcal{B}(\mathbf{c}_i, r)$ is diffeomorphic⁷ to a ball in \mathbb{R}^m [51]. For each U_i , we define ϕ_i to be the orthogonal projection to the tangent space of \mathcal{M} centered at c_i . According to [8, Lemma 2], ϕ_i is a diffeomorphism ⁸. We then let $\{(U_i, \phi_i)\}_{i=1}^{C_M}$ be an atlas on \mathcal{M} . The number of charts $C_{\mathcal{M}}$ is upper bounded by $C_{\mathcal{M}} \leq \left\lceil \frac{SA(\mathcal{M})}{r^m} T_m \right\rceil$ where $SA(\mathcal{M})$ is the surface area of \mathcal{M} , and T_m is the thickness⁹ of the U_i 's. The thickness T_m scales approximately linear in m[12].

Step 2. Construction of the oracle encoder and decoder. For the atlas $\{(U_i, \phi_i)\}_{i=1}^{C_M}$, let $\{\rho_i\}_{i=1}^{C_{\mathcal{M}}}$ be a C^{∞} partition of unity associated with $\{U_i\}_{i=1}^{C_{\mathcal{M}}}$ such that for each i, ρ_i is supported within U_i and each ρ_i is a C^{∞} function. The existence of such partition of unity is guaranteed by Proposition 1 [65].

We define the oracle encoder $\mathcal{E}^* : \mathcal{M} \to \mathbb{R}^{C_{\mathcal{M}}(d+1)}$ as

$$\mathcal{E}^*(\boldsymbol{u}) = \begin{bmatrix} \boldsymbol{f}_1(\boldsymbol{u}) & \cdots & \boldsymbol{f}_{C_{\mathcal{M}}}(\boldsymbol{u}) \end{bmatrix}^{\top}, \quad \text{with} \quad \boldsymbol{f}_j(\boldsymbol{u}) = \begin{bmatrix} (\phi_j(\boldsymbol{u}))^{\top} & \rho_j(\boldsymbol{u}) \end{bmatrix} \in \mathbb{R}^{m+1}, \quad (16)$$

and the corresponding oracle decoder $\mathcal{D}^* : \mathbb{R}^{C_{\mathcal{M}}(m+1)} \to \mathcal{M}$ as

$$\mathcal{D}^*(z) = \sum_{j=1}^{C_{\mathcal{M}}} \phi_j^{-1}((z_j)_{1:d}) \times (z_j)_{d+1}, \tag{17}$$

where $(z_j)_{1:d} = \begin{bmatrix} (z_j)_1 & \cdots & (z_j)_d \end{bmatrix}$. For any $u \in \mathcal{M}(q)$, one can verify that

$$\mathcal{D}^* \circ \mathcal{E}^*(oldsymbol{u}) = \sum_{j=1}^{C_{\mathcal{M}}} \phi_j^{-1} \circ \phi_j(oldsymbol{u}) imes
ho_j(oldsymbol{u}) = \sum_{oldsymbol{u} \in \operatorname{Supp}(
ho_j)} oldsymbol{u} imes
ho_j(oldsymbol{u}) = oldsymbol{u}.$$

• Encoder and decoder approximation theory. We next show that there exists networks \mathcal{E}_{θ_e} and \mathcal{D}_{θ_d} approximating \mathcal{E}^* and \mathcal{D}^* so that $\mathcal{D}_{\theta_d} \circ \mathcal{E}_{\theta_e}$ approximates $\mathcal{D}^* \circ \mathcal{E}^*$ with high accuracy. We will use the neural network approximation results in [70, 8].

Lemma 1 constructs a neural network to approximate the multiplication operation for bounded

Lemma 1 (Proposition 3 in [70]). For any B > 0 and $0 < \varepsilon < 1$, there exists a network $\widetilde{\times}$ so that for any $|x_1| \leq B$ and $|x_2| \leq B$, we have

$$|\widetilde{\times}(x_1, x_2) - x_1 \times x_2| < \varepsilon, \ \widetilde{\times}(x_1, 0) = \widetilde{\times}(0, x_2) = 0.$$

Such a network has $O(\log \varepsilon^{-1})$ layers and parameters. The width is bounded by 6 and all parameters are bounded by B^2 .

Lemma 2 constructs a neural network to universally approximate C^k functions (these functions have derivatives up to order k and all derivatives are bounded) on $[0,1]^d$.

 $^{^7}P$ is diffeomorphic to Q if there is a mapping $\Gamma: P \mapsto Q$ bijective, differentiable, and its inverse also being

 $^{^8\}phi_i$ is differentiable and its inverse ϕ_i^{-1} is also differentiable 9 Thickness is the average number of U_i 's that contain a point on \mathcal{M} [12].

Lemma 2 (Theorem 1 of [70]). Let M, F > 0. For any $\varepsilon \in (0,1)$, there is a network architecture $\mathcal{F}_{NN}(d,1,L,p,K,\kappa,M)$ with

$$L = O(\log \varepsilon^{-1}), \ p = O(\varepsilon^{-d/k}), \ K = O(\varepsilon^{-d/k} \log \varepsilon^{-1}), \ \kappa = O(\varepsilon^{-d/k})$$

so that for any C^k function $f^*: [0,1]^d \to [-M,M]$ with $\max_{\mathbf{k}:|\mathbf{k}| \le k} \sup_{\mathbf{x} \in [0,1]^d} |D^{\mathbf{k}} f^*| \le F$, there exists a network $f_{\mathrm{NN}} \in \mathcal{F}_{\mathrm{NN}}(d,1,L,p,K,\kappa,M)$ satisfying

$$||f_{\text{NN}} - f^*||_{L^{\infty}([0,1]^d)} \le \varepsilon.$$

The constants hidden in $O(\cdot)$ depend on d, k, M, F.

Lemma 3 constructs a neural network to universally approximate C^k functions (for an atlas, these functions have derivatives up to order k with respect to the local coordinates, and all derivatives are upper bounded) on manifold.

Lemma 3. Let \mathcal{M} be the manifold in Theorem 1. Let M, F > 0. For any $\varepsilon \in (0,1)$, there is a network architecture $\mathcal{F}_{NN}(n,1,L,p,K,\kappa,M)$ with

$$L = O(\log \varepsilon^{-1}), \ p = O(\varepsilon^{-m/k}), \ K = O(\varepsilon^{-m/k} \log \varepsilon^{-1}), \ \kappa = O(\varepsilon^{-m/k})$$

so that for any C^k function $f^*: \mathcal{M} \to [-M, M]$ with $\max_{\mathbf{k}: |\mathbf{k}| \le k} \sup_{\mathbf{x} \in [0,1]^d} |D^{\mathbf{k}} f^*| \le F^{10}$, there exists a network $f_{NN} \in \mathcal{F}_{NN}(n, 1, L, p, K, \kappa, M)$ satisfying

$$||f_{\rm NN} - f^*||_{L^{\infty}(\mathcal{M})} \le \varepsilon.$$

The constants hidden in $O(\cdot)$ depend on $m, k, \tau_M, F, M, B := \sup_{\boldsymbol{x} \in \mathcal{M}} \|\boldsymbol{x}\|_{\infty}$, n (linear), and the derivatives of the coordinate maps ϕ_i 's and the partition of unity ρ_i 's up to order k.

The encoder-decoder representation theory is guaranteed based on these neural network approximation lemmas.

Encoder approximation. For the oracle encoder \mathcal{E}^* in (16), each ϕ_j is a linear projection, so it can be realized by a linear layer in neural network. Each ρ_j is a C^{∞} function on \mathcal{M} . We apply Lemma 3 considering $\rho_j \in C^1$ and $\rho_j \in [0,1]$. Then For any $\varepsilon_{\rho_j} \in (0,1)$, there is a network architecture $\mathcal{F}_{NN}(n,1,L_{\rho_j},p_{\rho_j},K_{\rho_j},\kappa_{\rho_j},1)$ with

$$L_{\rho_j} = O(\log \varepsilon_{\rho_j}^{-1}), \ p_{\rho_j} = O(\varepsilon_{\rho_j}^{-m}), \ K_{\rho_j} = O(\varepsilon_{\rho_j}^{-m} \log \varepsilon_{\rho_j}^{-1}), \ \kappa_{\rho_j} = O(\varepsilon_{\rho_j}^{-m})$$

so that for the ρ_j in (16), there exists a network $\rho_{j,NN} \in \mathcal{F}_{NN}(n,1,L_{\rho_j},p_{\rho_j},K_{\rho_j},\kappa_{\rho_j},1)$ satisfying

$$\|\rho_{j,NN} - \rho_j\|_{L^{\infty}(\mathcal{M})} \le \varepsilon_{\rho_j}.$$

The constants hidden in $O(\cdot)$ depend on $m, k, \tau_M, B := \sup_{\boldsymbol{x} \in \mathcal{M}} \|\boldsymbol{x}\|_{\infty}$, n (linear), and the derivatives of the coordinate maps ϕ_i 's and the partition of unity ρ_i 's up to order 1.

With each ρ_j approximated by $\rho_{j,NN}$ above, we can put the networks indexed by $j = 1, ..., C_{\mathcal{M}}$ in parallel, and then obtain a network approximating \mathcal{E}^* in (16). Set $\varepsilon_{\rho_j} = \varepsilon_E$ for all j. Then there is a network architecture $\mathcal{F}_{NN}(n, C_{\mathcal{M}}(m+1), L_E, p_E, K_E, \kappa_E, M_E)$ with

$$L_E = O(\log \varepsilon_E^{-1}), \ p_E = O(C_{\mathcal{M}} \varepsilon_E^{-m}), \ K_E = O(C_{\mathcal{M}} \varepsilon_E^{-m} \log \varepsilon_E^{-1}), \ \kappa_E = O(\varepsilon_E^{-m}), \ M_E = O(1)$$

so that for the \mathcal{E}^* in (16), there exists a network $\mathcal{E}_{\theta_e} \in \mathcal{F}_{NN}(n, C_{\mathcal{M}}(m+1), L_E, p_E, K_E, \kappa_E, M_E)$

¹⁰These derivatives are defined on the coordinates for the atlas $\{U_i, \phi_i\}_{i=1}^{C_M}$.

satisfying

$$\sup_{\boldsymbol{u}\in\mathcal{M}}\|\mathcal{E}_{\theta_e}(\boldsymbol{u})-\mathcal{E}^*(\boldsymbol{u})\|_{\infty}\leq \varepsilon_E. \tag{18}$$

The constants hidden in $O(\cdot)$ depend on $m, \tau_{\mathcal{M}}, B := \sup_{\boldsymbol{u} \in \mathcal{M}} \|\boldsymbol{u}\|_{\infty}, n$ (linear), and the output, derivatives of the coordinate maps ϕ_i 's and the partition of unity ρ_i 's up to order 1.

Decoder approximation. For the oracle decoder \mathcal{D}^* in (17), we first approximate each $\phi_j^{-1}:\phi_j(U_j)\to\mathcal{M}\subset\mathbb{R}^n$, which is differentiable. We apply Lemma 2 for each output coordinate $(\phi_j^{-1})_k\in C^1$ for $k=1,\ldots,n$. For any $\varepsilon_{j,k}\in(0,1)$, there is a network architecture $\mathcal{F}_{\mathrm{NN}}(m,1,L_{j,k},p_{j,k},K_{j,k},\kappa_{j,k},B)$ with

$$L_{j,k} = O(\log \varepsilon_{j,k}^{-1}), \ p_{j,k} = O(\varepsilon_{j,k}^{-m}), \ K_{j,k} = O(\varepsilon_{j,k}^{-m} \log \varepsilon_{j,k}^{-1}), \ \kappa_{j,k} = O(\varepsilon_{j,k}^{-m})$$

so that for the $(\phi_j^{-1})_k : \phi_j(U_j) \to [-B, B]$, there exists a network $(\phi_j^{-1})_{k,NN} \in \mathcal{F}_{NN}(m, 1, L_{j,k}, p_{j,k}, K_{j,k}, \kappa_{j,k}, B)$ satisfying

$$\|(\phi_j^{-1})_{k,NN} - (\phi_j^{-1})_k\|_{L^{\infty}(\phi_j(U_j))} \le \varepsilon_{j,k}.$$
 (19)

The constants hidden in $O(\cdot)$ depend on $m, B := \sup_{\boldsymbol{x} \in \mathcal{M}} \|\boldsymbol{x}\|_{\infty}$, and the derivatives of the inverse coordinate maps ϕ_j^{-1} 's up to order 1.

After approximating the $(\phi_j^{-1})_k((\boldsymbol{z}_j)_{1:d})$ by $(\phi_j^{-1})_{k,\mathrm{NN}}((\boldsymbol{z}_j)_{1:d})$ in (17), we will approximate the multiplication operation $(\phi_j^{-1})_{k,\mathrm{NN}}((\boldsymbol{z}_j)_{1:d}) \times (\boldsymbol{z}_j)_{d+1}$ by a neural network according to Lemma 1. These quantities satisfy $|(\boldsymbol{z}_j)_{d+1}| \leq 1$ and $\sup_{(\boldsymbol{z}_j)_{1:d} \in \phi_j(U_j)} |(\phi_j^{-1})_{k,\mathrm{NN}}((\boldsymbol{z}_j)_{1:d})| \leq B$ for all j and k. For any $\varepsilon_M > 0$, the multiplication network for $\widetilde{\times} ((\phi_j^{-1})_{k,\mathrm{NN}}((\boldsymbol{z}_j)_{1:d}), (\boldsymbol{z}_j)_{d+1})$ such that

$$\left| \widetilde{\times} \left((\phi_j^{-1})_{k,\text{NN}}((\boldsymbol{z}_j)_{1:d}), (\boldsymbol{z}_j)_{d+1} \right) - (\phi_j^{-1})_{k,\text{NN}}((\boldsymbol{z}_j)_{1:d}) \times (\boldsymbol{z}_j)_{d+1} \right| \le \varepsilon_M$$
 (20)

has $O(\log \varepsilon_M^{-1})$ layers. The width is bounded by 6 and all parameters are bounded by B. Combining (19) and (20) gives rise to

$$\left|\widetilde{\times}\left((\phi_j^{-1})_{k,\mathrm{NN}}((\boldsymbol{z}_j)_{1:d}),(\boldsymbol{z}_j)_{d+1}\right)-(\phi_j^{-1})_k((\boldsymbol{z}_j)_{1:d})\times(\boldsymbol{z}_j)_{d+1}\right|\leq\varepsilon_M+\varepsilon_{j,k}$$

for each j and k. We set $\varepsilon_M/(2C_M)$ and $\varepsilon_{j,k} = \varepsilon_D/(2C_M)$, and then

$$\left|\sum_{j=1}^{C_{\mathcal{M}}} \widetilde{\times} \left((\phi_j^{-1})_{k,\mathrm{NN}}((\boldsymbol{z}_j)_{1:d}), (\boldsymbol{z}_j)_{d+1}\right) - \sum_{j=1}^{C_{\mathcal{M}}} (\phi_j^{-1})_k((\boldsymbol{z}_j)_{1:d}) \times (\boldsymbol{z}_j)_{d+1}\right| \leq \varepsilon_D$$

for all coordinate indexed by k.

In summary, for any $\varepsilon_D \in (0, 1)$, there is a network architecture $\mathcal{F}_{NN}(C_{\mathcal{M}}(m+1), n, L_D, p_D, K_D, \kappa_D, B)$ with

$$L_D = O(\log \varepsilon_D^{-1}), \ p_D = O(C_M \varepsilon_D^{-m}), \ K_D = O(C_M \varepsilon_D^{-m} \log \varepsilon_D^{-1}), \ \kappa_D = O(\varepsilon_D^{-m})$$
 (21)

so that for the oracle decoder $\mathcal{D}^* = \sum_{j=1}^{C_{\mathcal{M}}} \phi_j^{-1}((\boldsymbol{z}_j)_{1:d}) \times (\boldsymbol{z}_j)_{d+1}$ in (17), there exists a network $\mathcal{D}_{\theta_d} = \sum_{j=1}^{C_{\mathcal{M}}} \widetilde{\times} \left((\phi_j^{-1})_{k,\mathrm{NN}}((\boldsymbol{z}_j)_{1:d}), (\boldsymbol{z}_j)_{d+1} \right) \in \mathcal{F}_{\mathrm{NN}}(C_{\mathcal{M}}(m+1), n, L_D, p_D, K_D, \kappa_D, B)$ satisfying

$$\sup_{\{\boldsymbol{z}_j\}_{j=1}^{C_{\mathcal{M}}}:(\boldsymbol{z}_j)_{1:d}\in\phi_j(U_j),(\boldsymbol{z}_j)_{d+1}\in[0,1]} \|\mathcal{D}_{\theta_d}(\{\boldsymbol{z}_j\}_{j=1}^{C_{\mathcal{M}}}) - \mathcal{D}^*(\{\boldsymbol{z}_j\}_{j=1}^{C_{\mathcal{M}}})\|_{\infty} \leq \varepsilon_D.$$
(22)

The constants hidden in $O(\cdot)$ in (21) depend on $m, B := \sup_{\boldsymbol{u} \in \mathcal{M}} \|\boldsymbol{u}\|_{\infty}$, and the derivatives of the inverse coordinate maps ϕ_i^{-1} 's up to order 1.

• Propagator approximation theory. We next present the neural network approximation result for the latent propagator. The evolution from $\boldsymbol{u}(\boldsymbol{x},t,\boldsymbol{\zeta})$ to $\boldsymbol{u}(\boldsymbol{x},t+\tau,\boldsymbol{\zeta})$ is governed by the Lipschitz operator \mathfrak{F} . Let $\boldsymbol{z}(t,\boldsymbol{\zeta}) = \mathcal{E}^*(\boldsymbol{u}(t,\boldsymbol{\zeta}))$ and $\boldsymbol{z}(t+\tau,\boldsymbol{\zeta}) = \mathcal{E}^*(\boldsymbol{u}(\boldsymbol{x},t+\tau,\boldsymbol{\zeta}))$. With the oracle encoder \mathcal{E}^* and the oracle decoder \mathcal{D}^* on \mathcal{M} , there exists an oracle latent propagator \mathcal{P}^* such that

$$\mathcal{P}^*(\boldsymbol{z}(t,\boldsymbol{\zeta}),\tau,\boldsymbol{\zeta}) = \mathcal{E}^* \circ \mathfrak{F}(\mathcal{D}^*(\boldsymbol{z}(t,\boldsymbol{\zeta})),\tau,\boldsymbol{\zeta}). \tag{23}$$

With the oracle propagator in (23), the evolutionary operator \mathfrak{F} can be expressed as

$$u(x, t + \tau, \zeta) = \mathfrak{F}(u(x, t, \zeta)) = \mathcal{D}^* \circ \mathcal{P}^*(\mathcal{E}^*(u(x, t, \zeta), \tau, \zeta).$$

A workflow about the evolutionary operator, encoder, decoder and latent propagator is illustrated in Figure 16.

Figure 16: Workflow about the evolutionary operator, encoder, decoder and latent propagator.

Since the ϕ_j 's and ϕ_j^{-1} 's in (16) and (17) are differentiable, the oracle encoder \mathcal{E}^* and decoder \mathcal{D}^* are Lipschitz. We denote their Lipschitz constants by $\text{Lip}_{\mathcal{E}^*}$ and $\text{Lip}_{\mathcal{D}^*}$ so that $\|\mathcal{E}^*(\boldsymbol{u}_1) - \mathcal{E}^*(\boldsymbol{u}_2)\| \leq \text{Lip}_{\mathcal{E}^*}\|\boldsymbol{u}_1 - \boldsymbol{u}_2\|$ and $\|\mathcal{D}^*(\boldsymbol{z}_1) - \mathcal{D}^*(\boldsymbol{z}_2)\| \leq \text{Lip}_{\mathcal{D}^*}\|\boldsymbol{z}_1 - \boldsymbol{z}_2\|$. The Lipschitz constants $\text{Lip}_{\mathcal{E}^*}$ and $\text{Lip}_{\mathcal{D}^*}$ depend on the derivatives of the coordinate maps ϕ_i 's and the partition of unity ρ_i 's up to order 1. We claim that the oracle propagator in (23) is also Lipschitz: For $\boldsymbol{z}_1(t,\boldsymbol{\zeta}), \tau, \boldsymbol{\zeta} = \mathcal{E}^*(\boldsymbol{u}_1(\boldsymbol{x},t,\boldsymbol{\zeta}),\tau,\boldsymbol{\zeta})$ and $\boldsymbol{z}_2(t,\boldsymbol{\zeta}),\tau,\boldsymbol{\zeta} = \mathcal{E}^*(\boldsymbol{u}_2(\boldsymbol{x},t,\boldsymbol{\zeta}),\tau,\boldsymbol{\zeta})$, we have

$$\begin{split} &\|\mathcal{P}^*(\boldsymbol{z}_1(t,\boldsymbol{\zeta}),\tau,\boldsymbol{\zeta}) - \mathcal{P}^*(\boldsymbol{z}_2(t,\boldsymbol{\zeta}),\tau,\boldsymbol{\zeta})\| \\ &= \|\mathcal{E}^* \circ \mathfrak{F}(\boldsymbol{u}_1(\boldsymbol{x},t,\boldsymbol{\zeta}),\tau,\boldsymbol{\zeta}) - \mathcal{E}^* \circ \mathfrak{F}(\boldsymbol{u}_2(\boldsymbol{x},t,\boldsymbol{\zeta}),\tau,\boldsymbol{\zeta})\| \\ &\leq \operatorname{Lip}_{\mathcal{E}^*} \operatorname{Lip}_{\mathfrak{F}} \|\boldsymbol{u}_1 - \boldsymbol{u}_2\| \leq \operatorname{Lip}_{\mathcal{E}^*} \operatorname{Lip}_{\mathfrak{F}} \operatorname{Lip}_{\mathcal{D}^*} \|\boldsymbol{z}_1 - \boldsymbol{z}_2\|. \end{split}$$

The Lipschitz constant of \mathcal{P}^* satisfies $\operatorname{Lip}_{\mathcal{P}^*} \leq \operatorname{Lip}_{\mathcal{E}^*} \operatorname{Lip}_{\mathfrak{F}} \operatorname{Lip}_{\mathfrak{F}^*}$, which depends derivatives of the coordinate maps ϕ_i 's and ϕ_i^{-1} 's and the partition of unity ρ_i 's up to order 1. We next apply Lemma 2 for the approximation of $\mathcal{P}^*(\cdot, \tau, \zeta)$. For any $\varepsilon_P \in (0, 1)$, there is a network architecture $\mathcal{F}_{NN}(C_{\mathcal{M}}(m+1), C_{\mathcal{M}}(m+1), L_P, p_P, K_P, \kappa_P, M_P)$ with

$$L_P = O(\log \varepsilon_P^{-1}), \ p = O(\varepsilon_P^{-m}), \ K = O(\varepsilon_P^{-m} \log \varepsilon_P^{-1}), \ \kappa = O(\varepsilon_P^{-m}) \ M_P = O(1)$$

so that there exists a network $\mathcal{P}_{\theta_d} \in \mathcal{F}_{NN}(C_{\mathcal{M}}(m+1), C_{\mathcal{M}}(m+1), L_P, p_P, K_P, \kappa_P, M_P)$ satisfying

$$\sup_{\boldsymbol{z}(t,\boldsymbol{\zeta})\in\mathcal{E}^*(\mathcal{M})} \|\mathcal{P}_{\theta_d}(\boldsymbol{z}(t,\boldsymbol{\zeta}),\tau,\boldsymbol{\zeta}) - \mathcal{P}^*(\boldsymbol{z}(t,\boldsymbol{\zeta}),\tau,\boldsymbol{\zeta})\| \le \varepsilon_P, \tag{24}$$

for all t, τ, ζ . The constants hidden in $O(\cdot)$ depend on $C_{\mathcal{M}}, m$, the output and derivatives of the coordinate maps ϕ_i 's and ϕ_i^{-1} 's and the partition of unity ρ_i 's up to order 1.

• Putting the approximation of encoder, decoder and latent propagator together. Finally, we will put the neural network approximation result for the oracle encoder in (18), decoder in (22) and latent propagator in (24) together. With \mathcal{E}_{θ_e} approximating \mathcal{E}^* , \mathcal{D}_{θ_d} approximating \mathcal{D}^* ,

and \mathcal{P}_{θ_p} approximating \mathcal{P}^* , the evolutionary operator \mathfrak{F} can be approximated by \mathfrak{F}_{θ} as

$$\mathfrak{F}_{\theta}(\boldsymbol{u}(\boldsymbol{x},t,\boldsymbol{\zeta})) = \mathcal{D}_{\theta_d} \circ \mathcal{P}_{\theta_p}(\mathcal{E}_{\theta_e}(\boldsymbol{u}(\boldsymbol{x},t,\boldsymbol{\zeta}),\tau,\boldsymbol{\zeta}).$$

The approximation error of \mathfrak{F} is given as follows:

$$\begin{split} &\|\mathfrak{F}_{\theta}(\boldsymbol{u}(\boldsymbol{x},t,\boldsymbol{\zeta}))-\mathfrak{F}(\boldsymbol{u}(\boldsymbol{x},t,\boldsymbol{\zeta}))\|\\ &=\left\|\mathcal{D}_{\theta_{d}}\circ\mathcal{P}_{\theta_{p}}(\mathcal{E}_{\theta_{e}}(\boldsymbol{u}(\boldsymbol{x},t,\boldsymbol{\zeta}),\tau,\boldsymbol{\zeta})-\mathcal{D}^{*}\circ\mathcal{P}^{*}(\mathcal{E}^{*}(\boldsymbol{u}(\boldsymbol{x},t,\boldsymbol{\zeta}),\tau,\boldsymbol{\zeta})\right\|\\ &=\left\|\mathcal{D}_{\theta_{d}}\circ\mathcal{P}_{\theta_{p}}(\mathcal{E}_{\theta_{e}}(\boldsymbol{u}(\boldsymbol{x},t,\boldsymbol{\zeta}),\tau,\boldsymbol{\zeta})-\mathcal{D}_{\theta_{d}}\circ\mathcal{P}_{\theta_{p}}(\mathcal{E}^{*}(\boldsymbol{u}(\boldsymbol{x},t,\boldsymbol{\zeta}),\tau,\boldsymbol{\zeta})\right\|\\ &+\left\|\mathcal{D}_{\theta_{d}}\circ\mathcal{P}_{\theta_{p}}(\mathcal{E}^{*}(\boldsymbol{u}(\boldsymbol{x},t,\boldsymbol{\zeta}),\tau,\boldsymbol{\zeta})-\mathcal{D}_{\theta_{d}}\circ\mathcal{P}^{*}(\mathcal{E}^{*}(\boldsymbol{u}(\boldsymbol{x},t,\boldsymbol{\zeta}),\tau,\boldsymbol{\zeta})\right\|\\ &+\left\|\mathcal{D}_{\theta_{d}}\circ\mathcal{P}^{*}(\mathcal{E}^{*}(\boldsymbol{u}(\boldsymbol{x},t,\boldsymbol{\zeta}),\tau,\boldsymbol{\zeta})-\mathcal{D}^{*}\circ\mathcal{P}^{*}(\mathcal{E}^{*}(\boldsymbol{u}(\boldsymbol{x},t,\boldsymbol{\zeta}),\tau,\boldsymbol{\zeta})\right\|\\ &\leq \operatorname{Lip}_{\mathcal{D}_{\theta_{d}}}\operatorname{Lip}_{\mathcal{P}_{\theta_{p}}}\left\|\mathcal{E}_{\theta_{e}}(\boldsymbol{u}(\boldsymbol{x},t,\boldsymbol{\zeta})-\mathcal{E}^{*}(\boldsymbol{u}(\boldsymbol{x},t,\boldsymbol{\zeta}))\right\|+\operatorname{Lip}_{\mathcal{D}_{\theta_{d}}}\left\|\mathcal{P}_{\theta_{p}}(\mathcal{E}^{*}(\boldsymbol{u}(\boldsymbol{x},t,\boldsymbol{\zeta}),\tau,\boldsymbol{\zeta})-\mathcal{P}^{*}(\mathcal{E}^{*}(\boldsymbol{u}(\boldsymbol{x},t,\boldsymbol{\zeta}),\tau,\boldsymbol{\zeta})\right\|\\ &+\left\|\mathcal{D}_{\theta_{d}}\circ\mathcal{P}^{*}(\mathcal{E}^{*}(\boldsymbol{u}(\boldsymbol{x},t,\boldsymbol{\zeta}),\tau,\boldsymbol{\zeta})-\mathcal{D}^{*}\circ\mathcal{P}^{*}(\mathcal{E}^{*}(\boldsymbol{u}(\boldsymbol{x},t,\boldsymbol{\zeta}),\tau,\boldsymbol{\zeta})\right\|\\ &=\operatorname{Lip}_{\mathcal{D}_{\theta_{d}}}\operatorname{Lip}_{\mathcal{P}_{\theta_{p}}}\mathcal{E}_{E}+\operatorname{Lip}_{\mathcal{D}_{\theta_{d}}}\mathcal{E}_{P}+\mathcal{E}_{D}. \end{split}$$

Setting $\varepsilon_E = \varepsilon$, $\varepsilon_D = \varepsilon$ and $\varepsilon_P = \varepsilon$ yields Theorem 1.

B Training Dataset and Evaluation Strategy

The dataset is designed to facilitate single-shot multi-step prediction by capturing the temporal and parametric variations of the underlying PDE system. Each entry is organized as an ordered tuple:

$$(\boldsymbol{u}(\boldsymbol{x},t,\boldsymbol{\zeta}),\ \boldsymbol{u}(\boldsymbol{x},t+\tau,\boldsymbol{\zeta}),\ \tau,\ \boldsymbol{\zeta}),$$

where $u(x, t, \zeta) \in \mathbb{R}^n$ is the high-dimensional solution field, τ is the forecast horizon, and ζ denotes the system parameters (e.g., nondimensional quantities like Reynolds number). This formulation enables the model to learn the dynamics of the system across varying temporal and parametric configurations.

To ensure broad coverage, the dataset spans diverse values of ζ and τ , allowing the model to learn from a heterogeneous collection of system behaviors and forecasting challenges. The inclusion of arbitrary temporal offsets, as opposed to strictly consecutive snapshots, allows the model to internalize both short- and long-horizon dependencies.

This dataset design shares conceptual similarities with the Dynamic Mode Decomposition (DMD) framework [58], which also constructs input-output pairs to infer temporal evolution. However, while classical DMD is restricted to linear dynamics inferred from strictly consecutive snapshots (i.e., $\boldsymbol{u}(t), \boldsymbol{u}(t+\Delta t)$), our construction generalizes this by (i) permitting arbitrary temporal offsets τ and (ii) embedding the solution into a nonlinear latent space where dynamics are propagated via a learned, parameter-conditioned nonlinear map. These enhancements allow for more expressive modeling of complex temporal behaviors and improved generalization across parameterized regimes.

The dataset can be organized in matrix form as follows, where each row corresponds to a tuple containing the input state, its future state after a forecast horizon, the horizon itself, and the

associated parameters:

$$\mathcal{D} = \left[egin{array}{ccccc} oldsymbol{u}(oldsymbol{x},t_{11},oldsymbol{\zeta}_1) & oldsymbol{\tau}_{1JI} & oldsymbol{\zeta}_1 & oldsymbol{\zeta}_1 & oldsymbol{\zeta}_1 & oldsymbol{u}(oldsymbol{x},t_{11},oldsymbol{\zeta}_1) & oldsymbol{\tau}_{1JI} & oldsymbol{\zeta}_1 & oldsymbol{\tau}_{1JI} & oldsymbol{\zeta}_1 & oldsymbol{u}(oldsymbol{x},t_{11},oldsymbol{\zeta}_2) & oldsymbol{\tau}_{211} & oldsymbol{\zeta}_2 & oldsymbol{\varepsilon}_1 & oldsymbol{\varepsilon}_2 & oldsymbol{\varepsilon}_1 & oldsymbol{\varepsilon}_2 & oldsymbol{\varepsilon}_1 & oldsymbol{\varepsilon}_2 &$$

In the matrix above, the subscripts indicate indexing over different dimensions of the dataset: k = 1, ..., K indexes the distinct parameter configurations ζ_k , j = 1, ..., J indexes the initial times t_{kj} sampled for each configuration, i = 1, ..., I indexes the prediction horizons τ_{kji} applied to each initial time. Each row thus represents a training tuple consisting of a high-dimensional state $u(x, t_{kj}, \zeta_k)$, its future state after time τ_{kji} , the forecast horizon τ_{kji} , and the governing parameters ζ_k .

To evaluate generalization performance, the dataset is first partitioned into training and validation sets using a 70-30 split across the parameter space. The validation set is then further categorized into three distinct regions based on the joint distribution of the system parameters ζ and the forecast horizon τ . The first category, referred to as Left Extrapolation, includes parameter-time combinations where both ζ and τ lie below the range observed in the training data. The second category, Interpolation, encompasses combinations that fall within the convex hull of the training distribution, representing in-distribution generalization. The third category, Right Extrapolation, contains parameter-time pairs that exceed the upper bounds encountered during training. This stratified validation setup enables a rigorous assessment of the model's capacity to interpolate within known regimes and extrapolate beyond them.

This segmentation reflects scenarios where the model must interpolate within familiar conditions or extrapolate to previously unseen dynamics—emulating real-world deployment where coverage of all operating regimes is impractical. The strategy is illustrated in Fig. 17, where regions of training and validation are delineated across the joint $\tau - \zeta$ space.

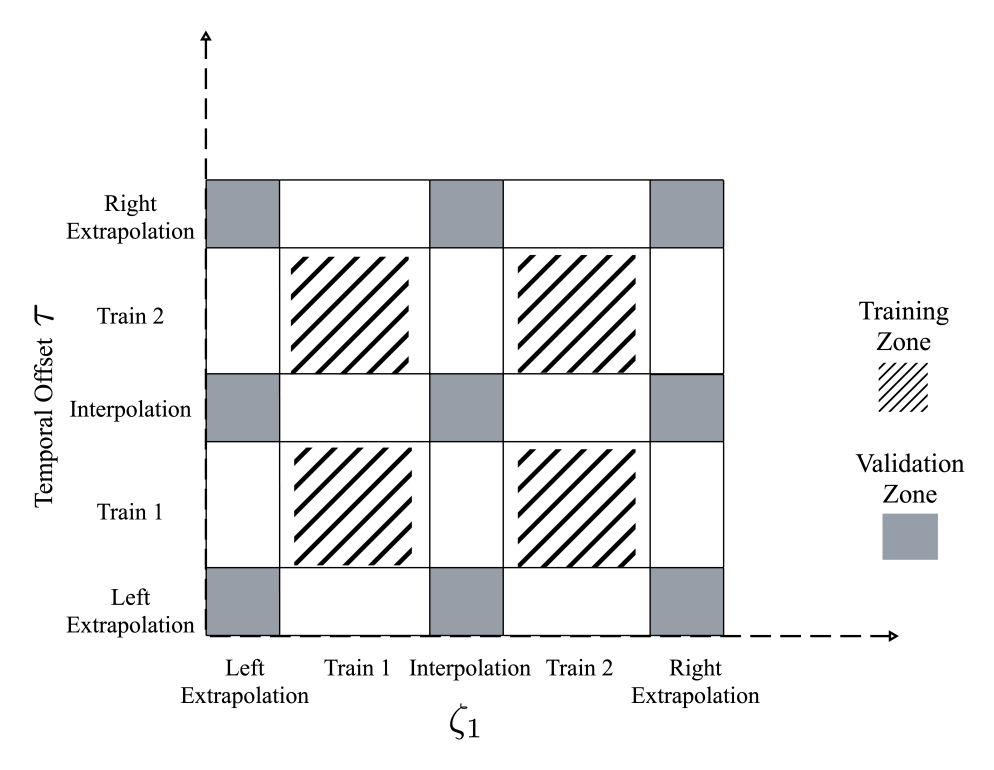


Figure 17: Data splitting strategy across parameter ζ_1 and forecast horizon τ . The shaded region indicates the training set, while extrapolation and interpolation zones are defined for validation.

Model performance is quantitatively evaluated using the L_2 norm of the prediction error as $\|\hat{\boldsymbol{u}}(\boldsymbol{x},t+\tau,\boldsymbol{\zeta})-\boldsymbol{u}(\boldsymbol{x},t+\tau,\boldsymbol{\zeta})\|_2$. Additionally, qualitative inspection of the predicted solutions is performed to assess fidelity in capturing critical features such as sharp gradients, nonlinear interactions, and wavefront propagation.

C Hyperparameter Optimization

Hyperparameter tuning was performed using Bayesian optimization via the wandb platform. The objective was to identify model configurations that balance reconstruction fidelity with accurate long-horizon forecasting across varying parametric regimes.

For both the Positional Encoding Propagator (PEP) and the Direct Concatenation Propagator (DCP), the search spanned key architectural and training hyperparameters: learning rate, batch size, number of epochs, KL-divergence weight (β) , and propagation loss weight (η) . The latent dimension was fixed at m=2, consistent with the intrinsic dimensionality analysis described in Section 3.1. Table 3 summarizes the range of values explored during optimization.

Table 3: Hyperparameter search space for the Burgers' equation experiments.

Parameter	Range
Learning rate (α)	$[1 \times 10^{-4}, \ 1 \times 10^{-3}]$
Batch size (B)	$\{64, 128, 256\}$
Number of epochs	$\{50, 100, 150\}$
KL-divergence weight (β)	$[1 \times 10^{-5}, 5 \times 10^{-2}]$
Propagation loss weight (η)	[0.5, 4.0]

In the case of the 2D advection-diffusion system, a separate tuning strategy was adopted to accommodate the increased complexity of the spatiotemporal dynamics and input dimensionality. The corresponding hyperparameter ranges are listed in Table 4.

Table 4: Hyperparameter search space for the advection-diffusion equation.

Parameter	Range
Learning rate (α)	$[1 \times 10^{-5}, \ 1 \times 10^{-3}]$
Number of epochs	$\{50, 75\}$
KL-divergence weight (β)	$[1 \times 10^{-4}, \ 1 \times 10^{-3}]$
Propagation loss weight (η)	[1.0, 4.5]

This systematic tuning process enabled robust configurations for each propagator, balancing generalization and accuracy across different data regimes. The final selected values for the Burgers' and advection-diffusion equation are reported in Table 1 and 2 of the main text, respectively.

D AE-LSTM Benchmark

This section provides additional technical details of the Autoencoder–Long Short-Term Memory (AE-LSTM) framework used as a comparative benchmark in our study. The AE-LSTM model follows a modular design where dimensionality reduction is first achieved through a nonlinear autoencoder, and the temporal evolution of the latent space is modeled using a recurrent sequence model conditioned on the Reynolds number (Re).

The AE-LSTM consists of three main components: an encoder network, a decoder network, and a two-layer LSTM. The encoder compresses a 128-dimensional spatial state into a 2-dimensional latent space. The LSTM is trained to evolve these latent representations over time, while the decoder reconstructs the full-order state from the predicted latent vectors. The LSTM operates

autoregressively in the latent space, with a prediction window of 40 input snapshots and iterative forecasting used to reach the desired time offset τ . The architecture is summarized in Table 5.

Table 5: Architecture of the AE-LSTM framework.

Component	Description
Encoder	Fully connected layers: [512, 256, 128, 64, 32], mapping the
	128-dimensional input to a 2D latent vector.
Decoder	Symmetric to the encoder; reconstructs the high-dimensional
	state from the latent representation.
LSTM	Two-layer LSTM; input dimension $= 3$ (2 latent variables $+$
	1 Reynolds number), hidden dimension = 40, output = 2D
	latent vector at next time step.

The autoencoder and LSTM are trained separately with details listed in Table 6. The autoencoder is trained using a reconstruction loss between the original high-dimensional state and the output of the decoder. The LSTM is trained using the mean squared error between predicted latent trajectories and ground-truth latent sequences obtained from the encoder. The training set consists of simulations for Reynolds numbers Re = [600, 625, ..., 2225]. The training data is normalized using min-max scaling across each spatial point. The decoder is only used after LSTM-based latent prediction to reconstruct the high-dimensional output. No regularization or dropout was applied, as early stopping based on validation loss prevented overfitting. Testing was performed on unseen Reynolds numbers including extrapolative and interpolative regimes.

Table 6: Training hyperparameters for AE and LSTM components.

Hyperparameter	AE	LSTM
Epochs	500	2000
Learning Rate	0.0003	0.00005
Batch Size	32	32
Optimizer	Adam	Adam $(\beta_1 = 0.9, \beta_2 = 0.999)$
Latent Dimension	2	
Hidden Dimension	_	40

References

- [1] E. Aamari, J. Kim, F. Chazal, B. Michel, A. Rinaldo, and L. Wasserman. Estimating the reach of a manifold. 2019.
- [2] I. Akhtar, A. H. Nayfeh, and C. J. Ribbens. On the stability and extension of reduced-order Galerkin models in incompressible flows: a numerical study of vortex shedding. *Theoretical and Computational Fluid Dynamics*, 23(3):213–237, 2009.
- [3] Y. Bengio, A. Courville, and P. Vincent. Representation learning: A review and new perspectives. *IEEE Transactions on Pattern Analysis and Machine Intelligence*, 35:1798–1828, 2013.
- [4] Y. Bengio, G. Mesnil, Y. Dauphin, and S. Rifai. Better mixing via deep representations. arXiv preprint arXiv:1207.4404, 2012.
- [5] S. L. Brunton, B. R. Noack, and P. Koumoutsakos. Machine learning for fluid mechanics. *Annual Review of Fluid Mechanics*, 52:477–508, 2020.
- [6] P. Campadelli, E. Casiraghi, C. Ceruti, and A. Rozza. Intrinsic dimension estimation: Relevant techniques and a benchmark framework. *Mathematical Problems in Engineering*, 2015(1):759567, 2015.

- [7] A. Chatterjee. An introduction to the proper orthogonal decomposition. *Current Science*, 78(7):808–817, 2000.
- [8] M. Chen, H. Jiang, W. Liao, and T. Zhao. Efficient approximation of deep relu networks for functions on low dimensional manifolds. Advances in neural information processing systems, 32, 2019.
- [9] M. Chen, H. Jiang, W. Liao, and T. Zhao. Nonparametric regression on low-dimensional manifolds using deep relu networks: Function approximation and statistical recovery. *Information and Inference: A Journal of the IMA*, 11(4):1203–1253, 2022.
- [10] J. Chung, K. Kastner, L. Dinh, K. Goel, A. Courville, and Y. Bengio. A recurrent latent variable model for sequential data. Advances in Neural Information Processing Systems (NeurIPS), 2015.
- [11] A. Cohen and R. DeVore. Approximation of high-dimensional parametric pdes. *Acta Numerica*, 24:1–159, 2015.
- [12] J. Conway and N. Sloane. Sphere packings, lattices and groups, volume 290. Springer Science & Business Media, 2013.
- [13] P. Del Moral. Nonlinear filtering: Interacting particle resolution. Comptes Rendus de l'Académie des Sciences Series I Mathematics, 325(6):653-658, 1997.
- [14] N. A. K. Doan, W. Polifke, and L. Magri. Auto-encoded reservoir computing for turbulence learning. arXiv preprint arXiv:2012.10968, 2020.
- [15] H. Eivazi, H. Veisi, M. H. Naderi, and V. Esfahanian. Deep neural networks for nonlinear model order reduction of unsteady flows. *Physics of Fluids*, 32(10):105104, 2020.
- [16] H. Federer. Curvature measures. Transactions of the American Mathematical Society, 93(3):418–491, 1959.
- [17] S. Fotiadis, M. L. Valencia, S. Hu, S. Garasto, C. D. Cantwell, and A. A. Bharath. Disentangled generative models for robust prediction of system dynamics. *Proceedings of the 40th International Conference on Machine Learning*, 202:10222–10248, 2023.
- [18] M. Fraccaro, S. Kamronn, U. Paquet, and O. Winther. A disentangled recognition and non-linear dynamics model for unsupervised learning. Advances in Neural Information Processing Systems (NeurIPS), 2017.
- [19] S. Fresca, L. Dede', and A. Manzoni. A comprehensive deep learning-based approach to reduced order modeling of nonlinear time-dependent parametrized pdes. *Journal of Scientific Computing*, 87:1–36, 2021.
- [20] D. J. Gauthier, E. Bollt, A. Griffith, and W. A. S. Barbosa. Next generation reservoir computing. arXiv preprint arXiv:2106.07688, 2021.
- [21] A. Glyn-Davies, C. Duffin, O. D. Akyildiz, and M. Girolami. φ-dvae: Physics-informed dynamical variational autoencoders for unstructured data assimilation. *Journal of Computational Physics*, 515:113293, 2024.
- [22] S. Godsill. Particle filtering: the first 25 years and beyond. In *Proc. Speech and Signal Processing (ICASSP) ICASSP 2019 2019 IEEE Int. Conf. Acoustics*, pages 7760–7764, 2019.

- [23] I. Higgins, L. Matthey, A. Pal, C. Burgess, X. Glorot, M. Botvinick, S. Mohamed, and A. Lerchner. β -vae: Learning basic visual concepts with a constrained variational framework. *ICLR* 2017 Poster, 2017.
- [24] G. E. Hinton and R. R. Salakhutdinov. Reducing the dimensionality of data with neural networks. *Science*, 313:504–507, 2006.
- [25] S. Hochreiter and J. Schmidhuber. Long short-term memory. *Neural Computation*, 9:1735–1780, 1997.
- [26] P. Holmes, J. L. Lumley, G. Berkooz, and C. W. Rowley. *Turbulence, Coherent Structures, Dynamical Systems and Symmetry*. Cambridge University Press, 2012.
- [27] R. E. Kalman. A new approach to linear filtering and prediction problems. *Journal of Basic Engineering*, 82(1):35–45, 1960.
- [28] H. R. Karbasian and W. M. van Rees. A parametric lstm neural network for predicting flow field dynamics across a design space. *Proceedings of the Royal Society A*, 481:20240055, 2025.
- [29] D. P. Kingma and J. Ba. Adam: A method for stochastic optimization. arXiv preprint arXiv:1412.6980, 2014.
- [30] D. P. Kingma and M. Welling. Auto-encoding variational bayes. arXiv preprint arXiv:1312.6114, 2013.
- [31] S. Kullback and R. A. Leibler. On information and sufficiency. *The annals of mathematical statistics*, 22(1):79–86, 1951.
- [32] J. N. Kutz, S. L. Brunton, B. W. Brunton, and J. L. Proctor. *Dynamic Mode Decomposition*. Society for Industrial and Applied Mathematics, Philadelphia, PA, 2016.
- [33] S. Le Clainche and J. M. Vega. Higher order dynamic mode decomposition. SIAM Journal on Applied Dynamical Systems, 16:882–925, 2017.
- [34] J. Lee. Riemannian manifolds: an introduction to curvature, volume 176. Springer Science & Business Media, 2006.
- [35] Y. Li and S. Mandt. Disentangled sequential autoencoder. *International Conference on Machine Learning (ICML)*, 2018.
- [36] Z. Li, N. Kovachki, K. Azizzadenesheli, B. Liu, K. Bhattacharya, A. Stuart, and A. Anand-kumar. Fourier neural operator for parametric partial differential equations. arXiv preprint arXiv:2010.08895, 2020.
- [37] H. Liu, B. Dahal, R. Lai, and W. Liao. Generalization error guaranteed auto-encoder-based nonlinear model reduction for operator learning. *Applied and Computational Harmonic Analysis*, 74:101717, 2025.
- [38] H. Liu, A. Havrilla, R. Lai, and W. Liao. Deep nonparametric estimation of intrinsic data structures by chart autoencoders: Generalization error and robustness. *Applied and Computational Harmonic Analysis*, 68:101602, 2024.
- [39] R. Lopez and P. J. Atzberger. Variational autoencoders for learning nonlinear dynamics of physical systems. arXiv preprint arXiv:2012.03448, 2020.

- [40] R. Lopez and P. J. Atzberger. Gd-vaes: Geometric dynamic variational autoencoders for learning nonlinear dynamics and dimension reductions. arXiv preprint arXiv:2206.05183, 2024.
- [41] L. Lu, P. Jin, and G. E. Karniadakis. Deeponet: Learning nonlinear operators for identifying differential equations based on the universal approximation theorem of operators. arXiv preprint arXiv:1910.03193, 2019.
- [42] B. Lukas. Experiment tracking with weights and biases. https://www.wandb.com, 2020.
- [43] Z. Luo, L. Wang, J. Xu, M. Chen, J. Yuan, and A. C. Tan. Flow reconstruction from sparse sensors based on reduced-order autoencoder state estimation. *Physics of Fluids*, 35, 2023.
- [44] R. Maulik, B. Lusch, and P. Balaprakash. Reduced-order modeling of advection—dominated systems with recurrent neural networks and convolutional autoencoders. *Physics of Fluids*, 33, 2021.
- [45] M. A. Mendez, M. Balabane, and J. M. Buchlin. Multi-scale proper orthogonal decomposition (mpod). *Physics of Fluids*, 30:055109, 2018.
- [46] M. Milano and P. Koumoutsakos. Neural network modeling for near wall turbulent flow. Journal of Computational Physics, 182:1–26, 2002.
- [47] F. Moukalled, L. Mangani, M. Darwish, F. Moukalled, L. Mangani, and M. Darwish. *The finite volume method.* Springer, 2016.
- [48] T. Murata, K. Fukami, and K. Fukagata. Nonlinear mode decomposition with convolutional neural networks for fluid dynamics. *Journal of Fluid Mechanics*, 882:A13, 2020.
- [49] R. Nakada and M. Imaizumi. Adaptive approximation and generalization of deep neural network with intrinsic dimensionality. *Journal of Machine Learning Research*, 21(174):1–38, 2020.
- [50] T. Nakamura, K. Fukami, K. Hasegawa, Y. Nabae, and K. Fukagata. Convolutional neural network and long short-term memory based reduced order surrogate for minimal turbulent channel flow. *Physics of Fluids*, 33(2):025116, 2021.
- [51] P. Niyogi, S. Smale, and S. Weinberger. Finding the homology of submanifolds with high confidence from random samples. *Discrete & Computational Geometry*, 39:419–441, 2008.
- [52] S. E. Otto, G. R. Macchio, and C. W. Rowley. Learning nonlinear projections for reduced-order modeling of dynamical systems using constrained autoencoders. arXiv preprint arXiv:2307.15288, 2023.
- [53] M. Raissi, P. Perdikaris, and G. E. Karniadakis. Physics-informed neural networks: A deep learning framework for solving forward and inverse problems involving nonlinear partial differential equations. *Journal of Computational Physics*, 378:686–707, 2019.
- [54] N. A. Raj, D. Tafti, and N. Muralidhar. Comparison of reduced order models based on dynamic mode decomposition and deep learning for predicting chaotic flow in a random arrangement of cylinders. *Physics of Fluids*, 35, 2023.
- [55] C. W. Rowley and S. T. M. Dawson. Model reduction for flow analysis and control. *Annual Review of Fluid Mechanics*, 49:387–417, 2017.
- [56] C. Roy. Review of discretization error estimators in scientific computing. In 48th AIAA Aerospace Sciences Meeting Including the New Horizons Forum and Aerospace Exposition, page 126, 2010.

- [57] P. J. Schmid. Dynamic mode decomposition of numerical and experimental data. *Journal of Fluid Mechanics*, 656:5–28, 2010.
- [58] P. J. Schmid. Dynamic mode decomposition and its variants. *Annual Review of Fluid Mechanics*, 54(1):225–254, 2022.
- [59] J. Schmidt-Hieber. Nonparametric regression using deep neural networks with relu activation function. *The Annals of Statistics*, 48(4):1875–1897, 2020.
- [60] S. Shakya, B. Maharjan, and P. Shakya. From entanglement to disentanglement: Comparing traditional vae and modified beta-vae performance. *International Journal on Engineering Technology*, 2(1), 2024.
- [61] M. Sieber, C. O. Paschereit, and K. Oberleithner. Spectral proper orthogonal decomposition. *Journal of Fluid Mechanics*, 792:798–828, 2016.
- [62] A. Solera-Rico, C. S. Vila, M. A. Gómez, Y. Wang, A. Almashjary, S. T. M. Dawson, and R. Vinuesa. β-variational autoencoders and transformers for reduced-order modelling of fluid flows. arXiv preprint arXiv:2304.03571, 2023.
- [63] P. A. Srinivasan, L. Guastoni, H. Azizpour, P. Schlatter, and R. Vinuesa. Predictions of turbulent shear flows using deep neural networks. *Physical Review Fluids*, 4:054603, 2019.
- [64] J. H. Tu, C. W. Rowley, D. M. Luchtenburg, S. L. Brunton, and J. N. Kutz. On dynamic mode decomposition: Theory and applications. *Journal of Computational Dynamics*, 2014.
- [65] L. Tu. Manifolds. In An Introduction to Manifolds, pages 47–83. Springer, 2011.
- [66] R. Van Der Merwe, A. Doucet, N. De Freitas, and E. Wan. The unscented particle filter. In Proceedings of the 13th International Conference on Neural Information Processing Systems, NIPS'00, pages 563–569, Cambridge, MA, USA, 2000. MIT Press.
- [67] A. Vaswani, N. Shazeer, N. Parmar, J. Uszkoreit, L. Jones, A. N. Gomez, L. Kaiser, and I. Polosukhin. Attention is all you need. arXiv preprint arXiv:1706.03762, 2017.
- [68] E. A. Wan and R. Van Der Merwe. The unscented kalman filter for nonlinear estimation. In Proceedings of the IEEE 2000 Adaptive Systems for Signal Processing, Communications, and Control Symposium (Cat. No.00EX373), pages 153–158, 2000.
- [69] Z. Wang, D. Xiao, F. Fang, R. Govindan, C. Pain, and Y. Guo. Model identification of reduced order fluid dynamics systems using deep learning. *International Journal for Numerical Methods in Fluids*, 86(4):255–268, 2018.
- [70] D. Yarotsky. Error bounds for approximations with deep relu networks. *Neural networks*, 94:103–114, 2017.
- [71] B. Zhang. Nonlinear mode decomposition via physics-assimilated convolutional autoencoder for unsteady flows over an airfoil. *Physics of Fluids*, 35, 2023.
- [72] W. Zhong and H. Meidani. PI-VAE: Physics-informed variational auto-encoder for stochastic differential equations. *ArXiv preprint arXiv:2203.11363*, 2022.
- [73] O. C. Zienkiewicz, R. L. Taylor, and J. Zhu. The finite element method: its basis and fundamentals. Elsevier, 2005.